



HAL
open science

A Numerical Model of the SEIS Leveling System Transfer Matrix and Resonances: Application to SEIS Rotational Seismology and Dynamic Ground Interaction

Lucile Fayon, Brigitte Knapmeyer-Endrun, Philippe Lognonné, Marco Bierwirth, Aron Kramer, Pierre Delage, Foivos Karakostas, Sharon Kedar, Naomi Murdoch, Nicolas Verdier, et al.

► **To cite this version:**

Lucile Fayon, Brigitte Knapmeyer-Endrun, Philippe Lognonné, Marco Bierwirth, Aron Kramer, et al.. A Numerical Model of the SEIS Leveling System Transfer Matrix and Resonances: Application to SEIS Rotational Seismology and Dynamic Ground Interaction. *Space Science Reviews*, 2018, 214 (119), pp.1-39. 10.1007/s11214-018-0555-9 . hal-01990999

HAL Id: hal-01990999

<https://hal.science/hal-01990999v1>

Submitted on 23 Jan 2019

HAL is a multi-disciplinary open access archive for the deposit and dissemination of scientific research documents, whether they are published or not. The documents may come from teaching and research institutions in France or abroad, or from public or private research centers.

L'archive ouverte pluridisciplinaire **HAL**, est destinée au dépôt et à la diffusion de documents scientifiques de niveau recherche, publiés ou non, émanant des établissements d'enseignement et de recherche français ou étrangers, des laboratoires publics ou privés.



Open Archive Toulouse Archive Ouverte (OATAO)

OATAO is an open access repository that collects the work of some Toulouse researchers and makes it freely available over the web where possible.

This is an author's version published in: <https://oatao.univ-toulouse.fr/21697>

Official URL : <https://doi.org/10.1007/s11214-018-0555-9>

To cite this version :

Fayon, Lucile and Knapmeyer-Endrun, Brigitte and Lognonné, Philippe,... [et al.]. A Numerical Model of the SEIS Leveling System Transfer Matrix and Resonances: Application to SEIS Rotational Seismology and Dynamic Ground Interaction. (2018) Space Science Reviews, 214 (119). 1-39. ISSN 0038-6308

Any correspondence concerning this service should be sent to the repository administrator:

tech-oatao@listes-diff.inp-toulouse.fr

A Numerical Model of the SEIS Leveling System Transfer Matrix and Resonances: Application to SEIS Rotational Seismology and Dynamic Ground Interaction

Lucile Fayon¹ · Brigitte Knapmeyer-Endrun² · Philippe Lognonné¹ ·
Marco Bierwirth³ · Aron Kramer³ · Pierre Delage⁴ · Foivos Karakostas¹ ·
Sharon Kedar⁵ · Naomi Murdoch⁶ · Raphael F. Garcia⁶ · Nicolas Verdier⁷ ·
Sylvain Tillier¹ · William T. Pike⁸ · Ken Hurst⁵ · Cédric Schmelzbach⁹ ·
William B. Banerdt⁵

Abstract Both sensors of the SEIS instrument (VBBs and SPs) are mounted on the mechanical leveling system (LVL), which has to ensure a level placement on the Martian ground under currently unknown local conditions, and provide the mechanical coupling of the seismometers to the ground. We developed a simplified analytical model of the LVL structure in order to reproduce its mechanical behavior by predicting its resonances and transfer function. This model is implemented numerically and allows to estimate the effects of the LVL on the data recorded by the VBBs and SPs on Mars. The model is validated through comparison with the horizontal resonances (between 35 and 50 Hz) observed in laboratory measurements. These modes prove to be highly dependent of the ground horizontal stiffness and torque. For this reason, an inversion study is performed and the results are compared with some experimental measurements of the LVL feet's penetration in a martian regolith analog. This comparison shows that the analytical model can be used to estimate the elastic ground

✉ L. Fayon
fayon@ipgp.fr

¹ Institut de Physique du Globe de Paris-Sorbonne Paris Cité, Université Paris Diderot, Paris, France

² Earthquake Observatory Bensberg, University of Cologne, Bergish Gladbach, Germany

³ Max Planck Institute for Solar System Research, Göttingen, Germany

⁴ Laboratoire Navier (CERMES), Ecole des Ponts ParisTech, Paris, France

⁵ Jet Propulsion Laboratory (JPL), California Institut of Technology, Pasadena, CA, USA

⁶ Institut Supérieur de l'Aéronautique et de l'Espace (ISAE-SUPAERO), Université de Toulouse, 31400 Toulouse, France

⁷ Centre National d'Etudes Spatiales (CNES), Toulouse, France

⁸ Imperial College, London, United Kingdom

⁹ ETH, Zurich, Switzerland

properties of the InSight landing site. Another application consists in modeling the 6 sensors on the LVL at their real positions, also considering their sensitivity axes, to study the performances of the global SEIS instrument in translation and rotation. It is found that the high frequency ground rotation can be measured by SEIS and, when compared to the ground acceleration, can provide ways to estimate the phase velocity of the seismic surface waves at shallow depths. Finally, synthetic data from the active seismic experiment made during the HP³ penetration and SEIS rotation noise are compared and used for an inversion of the Rayleigh phase velocity. This confirms the perspectives for rotational seismology with SEIS which will be developed with the SEIS data acquired during the commissioning phase after landing.

Keywords InSight · Mars · Regolith

1 Introduction

NASA's InSight mission, scheduled to land in November 2018, will for the first time perform a detailed, surface-based geophysical investigation of planet Mars. The primary goals of the mission are the determination of Mars' internal structure and thermal state in order to understand the fundamental processes guiding the formation and evolution of terrestrial planets, and the measurement of the present level of Mars' tectonic activity and the impact flux on the planet (Banerdt et al. 2013). The mission consists of a single lander, built by using operational experience inherited from Phoenix and MER (Mars Exploration Rover), upgraded with Juno and GRAIL (Gravity Recovery And Interior Laboratory) avionics. This lander carries two main payloads, SEIS (Seismic Experiment for Interior Structure) and HP³ (Heat flow and Physical Properties Probe), as well as auxiliary meteorological sensors, a magnetometer, two color cameras, and RISE (Rotation and Interior Structure Experiment), which will use the X-band communication link for precise Doppler tracking of the lander's location.

The SEIS instrument is composed of two independent three-axis seismometers: a Very Broad Band (VBB) and a MEMS (Micro-Electro-Mechanical System) short-period (SP) sensor (Lognonné et al. 2018). The measurement ranges of the two 3-axis seismometers partially overlap, allowing for some redundancy, inter-sensor cross-calibration, as well as measurements of the accelerations at the location of the 6 sensors. SEIS will accordingly measure seismic activity over a very broad frequency range, from 0.01 Hz up to 10 Hz and 0.1 Hz to 50 Hz for the VBBs and SPs respectively, extended to longer periods for the position output of the VBB (Lognonné and Pike 2015). Both sensors are mounted on the mechanical leveling system (LVL), on which the present study is focused. The complete SEIS sensor assembly will be placed on the Martian ground by a robotic arm after landing, and a Wind and Thermal Shield (WTS) will protect it from Martian weather and direct solar radiation. The purpose of the LVL is two-fold: it will level the SEIS sensors on the Martian ground under currently unknown local conditions, a requirement that needs to be fulfilled for proper operation of the highly sensitive VBB seismometer, and subsequently help to monitor the tilt of the sensor assembly. In addition, it will provide the mechanical coupling of the seismometers to the ground. The direct placement of SEIS on the Martian surface comprises a huge improvement compared to the only previous seismic experiment on Mars performed during the Viking missions (Anderson et al. 1977): the Viking seismometers were located on top of their respective lander decks, which induced a high level of noise due to wind-driven lander vibrations (Nakamura and Anderson 1979), and at the same time degraded the mechanical coupling of the seismometers to the ground. The deployment of

the seismometers directly on the Martian surface with the help of the LVL is expected to improve the quality of the resulting seismic recordings significantly (Lognonné et al. 1996).

As all ground motion is transferred to the SEIS sensors via the LVL, it is important to understand its characteristics and possible influences on the recorded waveforms. Horizontal resonances of the LVL were observed in the laboratory during qualification tests at the subsystem and system level and occurred at frequencies between 35 and 50 Hz, depending on the LVL configuration. Here, we develop a simplified analytic model of the LVL structure that reproduces its mechanical behavior as accurately as possible in order to predict its transfer function and its effect on VBB and SP data recorded on Mars. As the transfer function, i.e. the frequencies and amplitudes of the horizontal resonances, depends not only on the LVL configuration, but also on the coupling between the LVL and the ground, the resonances observed in the seismograms from Mars will allow us to constrain the elastic properties of the shallow subsurface at the landing site. Additional information on subsurface properties can be derived by using HP³ signals and the spatial distribution of the six SEIS components on the LVL. The HP³ “mole”, a subsurface heat flow probe that will penetrate the Martian ground up to 5 m deep using a self-hammering mechanism, will generate thousands of seismic signals that will be recorded by SEIS (Kedar et al. 2017). The high frequencies of the mole-generated signals and the spatial distribution of the six SEIS sensors on the LVL permit the application of the principles of rotational seismology to SEIS by calculating the spatial derivatives of the wavefield (Spudich et al. 1995; Sollberger et al. 2018).

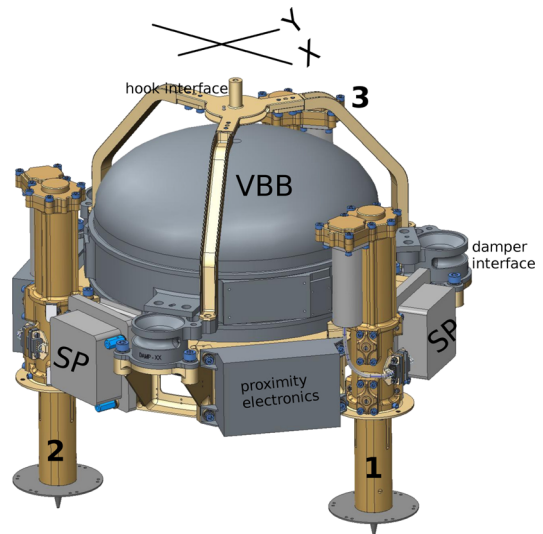
In this paper, we first provide details about the SEIS instrument and the LVL structure. Then, we describe the laboratory tests during the LVL resonances were observed. Afterwards, the model construction is presented with its validation process. Finally, we outline the different possible applications of the model. We conclude by explaining how the analytical LVL model will be applied when the instrument is deployed on Mars and by showing the performance of the combination of the six seismic sensors to obtain translational and rotational information, and, after additional analysis, the phase velocity of high frequency surface waves excited by the HP³ “mole”.

2 The SEIS Instrument and Its Leveling System

The LVL consists of a mechanical part, the leveling structure, which we model in detail here, and the motor drive electronics (MDE) board, that, in addition to commanding the LVL structure during leveling, can perform readings on two independent sets of tilt meters on the LVL. The main parts of the LVL structure are three linear actuator legs that hold a structural ring of 25 cm diameter (Fig. 1). The legs are screwed to the ring at two places near its upper and lower rim. They consist of a fixed outer tube and a movable inner tube that can be extracted and retracted up to 59 mm via motion along a spindle guided by a spring and ball bearing system within the leg (Lognonné et al. 2018). This allows for level placement of the sensor assembly on slopes of up to 15°, the maximum local ground tilt expected within the InSight landing ellipse (Golombek et al. 2017), by driving the legs independently. Both the VBB and SP sensors as well as their proximity electronics are mounted on the structural ring (Fig. 1) and contained within the Remote Warm Enclose Box (RWEB).

The VBB consists of three inverted mechanical pendulums which are kept in their mean positions using a magnetic force feedback in a closed loop (Lognonné et al. 2018; De Raucourt et al. 2012). The sensitivity axes (U, V, W) of the pendulums are inclined at 30 deg from the horizontal, and the sensors are located in an evacuated container with the center of

Fig. 1 Design drawing showing the complete instrument assembly including the LVL structure, VBB sphere, and SP boxes. Conventions for coordinate system and numbering of legs are indicated



gravity of the proof masses half way to the center of the structural ring at 120° separation from each other. The SP sensors, on the other hand, are mounted on the outside of the structural ring at 120° intervals at a distance of 21.65 cm from each other, with an SP sensor to the right of each LVL leg when viewed from the top (Fig. 1). The position of each sensor (VBBs and SPs) is represented in Fig. 2.

During cruise, the LVL is fixed on the lander deck by dampers attached to the structural ring that will be released before deployment. A hook interface on top of the LVL structure allows the grapple on the lander’s robotic arm to grab and deploy the sensor assembly on the ground (Fig. 1). The design of the LVL feet is based on penetration experiments in Martian regolith simulants performed at Ecole des Ponts ParisTech. The LVL feet need to provide a stable contact and good coupling between the SEIS instrument assembly and the Martian surface at the landing site, where a regolith cover consisting of cohesionless sand or low-cohesion soil with a very low percentage of rocks is expected (Golombek et al. 2017; Warner et al. 2017). Early on, it became clear that cone-shaped feet, as usual for Earth-based seismometers, can result in uncontrolled sinking if deployed on a sandy surface. To prevent sinking further than a pre-determined point and to provide better coupling, it was decided to add a round metal disk at the upper end of each foot (Fig. 1). The optimum dimensions of the foot cone were determined by dedicated measurements and tests, ensuring the full penetration of the cone in Mars simulant under the weight of SEIS under Martian gravity, and led to cones of 10 mm maximum diameter and 20 mm length.

When describing the horizontal orientation of the LVL, we use an X–Y reference coordinate system as indicated in Figs. 1 and 2. To distinguish between the individual legs, they are numbered clockwise, starting (LVL leg 1) at the interface for the tether cable at the structural ring (Fig. 2).

The effect of the LVL on SEIS recordings has previously been studied theoretically by regarding the filtering effect of the three-legged geometry on high-frequency signals generated by the HP³ (Kedar et al. 2017). Furthermore, Teanby et al. (2017) performed field experiments on basaltic sands in Iceland to investigate the transfer of wind noise from the WTS feet to the LVL feet and to SEIS through a regolith analogue at 5 Hz, using rigid tripods to simulate the WTS and the LVL, and an active spring source. This work was extended to

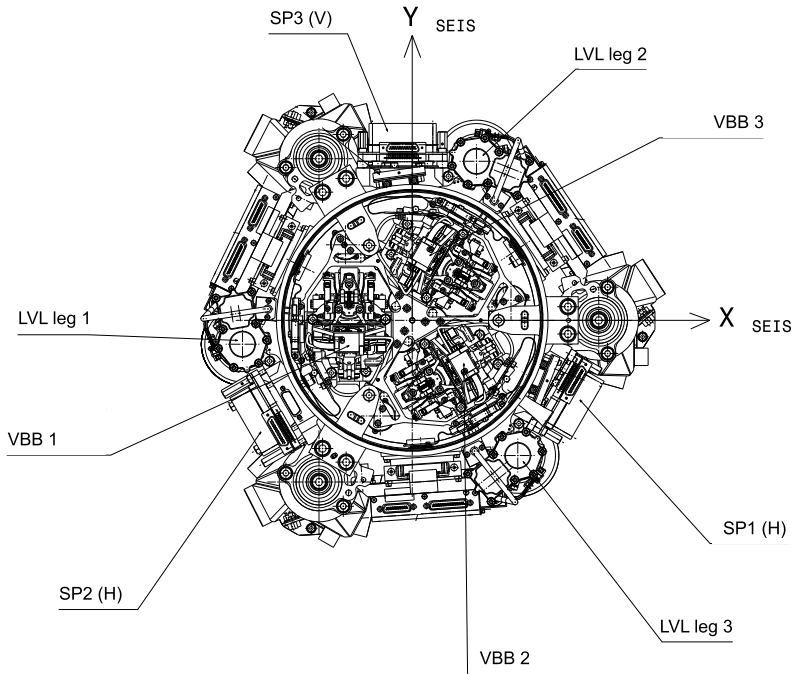


Fig. 2 Top view of the LVL structure around the sphere interior (CNES 2017). The X_{SEIS} and Y_{SEIS} axes, defined with respect to the SEIS hardware, are used in the model

a broader frequency range by Myhill et al. (2018), who observe an effect of the tripod on signal polarization as well as a vertical resonance at frequencies above 20 Hz attributed to forced harmonic oscillations of the tripod on unconsolidated regolith. However, these field experiments did not use an actual LVL including the movable legs, and were conducted with a mass of about one third the flight mass of the sensor assembly, a tripod leg spacing about 40% larger than that of the actual LVL, and differently shaped foot cones (almost twice as broad, but shorter). The lab tests described below used the actual LVL flight model (FM) for the most part, but had to be conducted in a clean environment, which prevented the use of a regolith analogue. The use of the actual LVL allows horizontal resonance effects unique to the structure to be observed, though, and some tests done with a qualification model (QM) on sand can provide at least an indication of any additional regolith effects not covered by the FM tests.

3 Observation of Resonances

Seismic testing and transfer function measurements of the LVL structure were done under different test scenarios, with an increasingly more complete integration of the system. Firstly, the resonances of the Load Shunt Assembly (LSA) were determined in different configurations of the Engineering Model (EM) of the LVL in a sand box. Then, the transfer functions were measured during forced excitation in dedicated measurements during vibration tests of the LVL structure FM at test facilities of DLR Bremen. Seismic transfer

Table 1 Summary of measurements of the LVL transfer function using ambient noise. The two representative measurements from the MPS data set that are used for the modeling described below are listed, as well as all measurements performed at CNES. The mass of the complete system and length of all three legs, measured from the tips of the feet to the point where the leg is screwed to the ring, as well as the resulting tilt in X and Y direction and the observed resonance frequencies in the two directions, f_x and f_y , are given. ^(*) indicates that SP sensors were used in the last experiment, so the measurement directions are not X and Y, but correspond to the orientation of the horizontal SPs with an angular difference of 120°

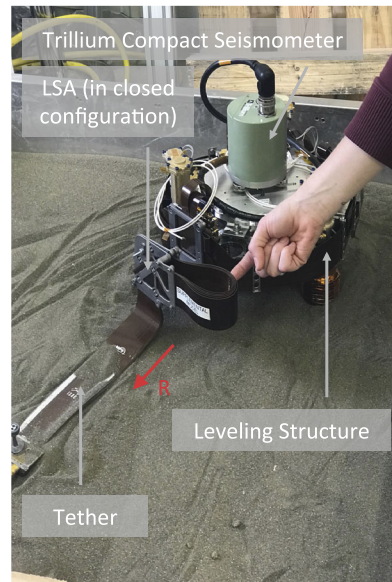
Location	Surface	Mass [g]	Length Leg 1 [mm]	Length Leg 2 [mm]	Length Leg 3 [mm]	Tilt X [deg]	Tilt Y [deg]	LSA status	f_x [Hz]	f_y [Hz]
MPS	Floor coating	9082	75.5	75.5	75.5	0	0	no LSA	45.4	45.4
MPS	Magmatic rock	9082	75.5	125.7	125.7	15	0	no LSA	36.5	34.7
CNES	Sand	8924	104.7	113.0	107.6	1.7	1.4	open	34.8	34.0
CNES	Sand	8924	89.4	121.4	112.9	8.4	2.2	open	33.0	30.9
CNES	Sand	8924	78.8	133.3	110.0	12.9	6.1	open	36.1	37.6
CNES	Aluminium	~9000	104.5	104.5	104.5	0	0	closed	40.2 ^(*)	40.1 ^(*)

functions were also determined using ambient vibrations as an excitation source for different configurations (different floor materials and leg extensions) of the LVL, described in Table 1. In the first two cases, the transfer function of the LVL FM was determined in the MPS (Max Planck Institute for Solar System Research) clean room on two different supports: the floor coating and a magmatic rock plate. In both scenarios, the measurements were done without the actual SEIS sensor assembly, so configurations deviate somewhat from the deployment on Mars. Another measurement of the seismic transfer function of the LVL FM, but not described in the table, was again made using ambient vibrations at CNES Toulouse for a single configuration, including further parts of the sensor assembly (tether with closed LSA, dampers, lower part of the RWEB enclosure), but a lower total mass. In the third measurement of Table 1, CNES Toulouse also performed three measurements at variable ground tilt with the LVL QM in a sand box. Again, the setup included the tether (but with the open LSA) and parts of the RWEB. Finally, the transfer function was also determined using the horizontal SP sensors installed on the LVL FM, including the VBB sphere, proximity electronics boxes, tether with closed LSA, dampers, and the lower part of RWEB. In the following, we briefly describe each of these sets of measurements and outline how the actual LVL transfer function can be determined when SEIS is deployed on Mars.

3.1 Determination of the Load Shunt Assembly Resonances

The load shunt assembly (LSA) is intended to mechanically decouple the seismometers from thermoelastic expansion and contraction of the tether providing the necessary connection to the electronics in the thermal enclosure of the lander. The tether cable is the electronic link between the lander and the SEIS instrument. In traversing from the lander to the LVL, the tether is subject to diurnal temperature variations exceeding 100 °C every sol. On Earth, standard broadband seismometer installation practice is to minimize the effect of the thermoelastic expansion of the tether by, first, having it subject to small (usually < 1 °C) temperature variations, and, second, wrap the cable around the seismometer at least 1 full turn before going into the seismometer. Neither of these conditions are possible on Mars. Hence two features were invented to minimize the effect of temperature changes in

Fig. 3 Picture of the experimental setup of the LVL EM with someone “plucking” the LSA



the tether. The first consists of a 250 g “pinning mass” attached to the tether just outside the WTS that is placed over the Sensor Assembly creating a small “vault” on the surface. The second consists of a compliant fold in the tether just where it enters the seismometer.

This compliant fold is held in place during transport with a breakable bolt. After the seismometer is placed on Mars, this bolt is broken and the fold of the LSA is opened. Its presence on the side of the seismometer introduces a suspended mass that induces resonances. To characterize the effect of the LSA, we plucked it with a finger (Fig. 3), and recorded the resulting signal on a Trillium Compact seismometer sitting on top of an aluminum plate bolted on the LVL EM.

The Trillium Compact seismometer data, shown in Fig. 4, was analyzed to determine the frequency of the LSA in both open and closed configurations. This is shown on Fig. 5. When the LSA is open, this seems to decrease and multiply the resonance frequency with a principal peak at 5.1 Hz on the vertical and transverse components and at 3.8 Hz for the radial component. This information have to be known for the interpretation of the seismic data on Mars.

3.2 Seismic Transfer Function Measurements on Shaker

The LVL FM seismic transfer function was first determined on a shaker with an input acceleration of 0.1 g (g being the earth gravity acceleration, equal to 9.8 m/s^2) using a sweep signal between 5 and 200 Hz with a sweep rate of two octaves per minute. The resulting acceleration at various points of the LVL was recorded with miniature accelerometers attached to the LVL structure with glue. The tips of the LVL feet were glued to the shaker’s metal table to prevent any motion between LVL and the table during vibration. A metal disk was screwed to the damper interface points, similar to where the VBB sphere is connected in the final SEIS setup, and the hook interface attached. The total mass of the system is 5300 g in this configuration. The LVL legs were extracted to an intermediate length comparable to the stowed configuration during cruise. Two measurements were conducted, one for acceleration in the X direction, and the other for acceleration in the Y direction, both directions

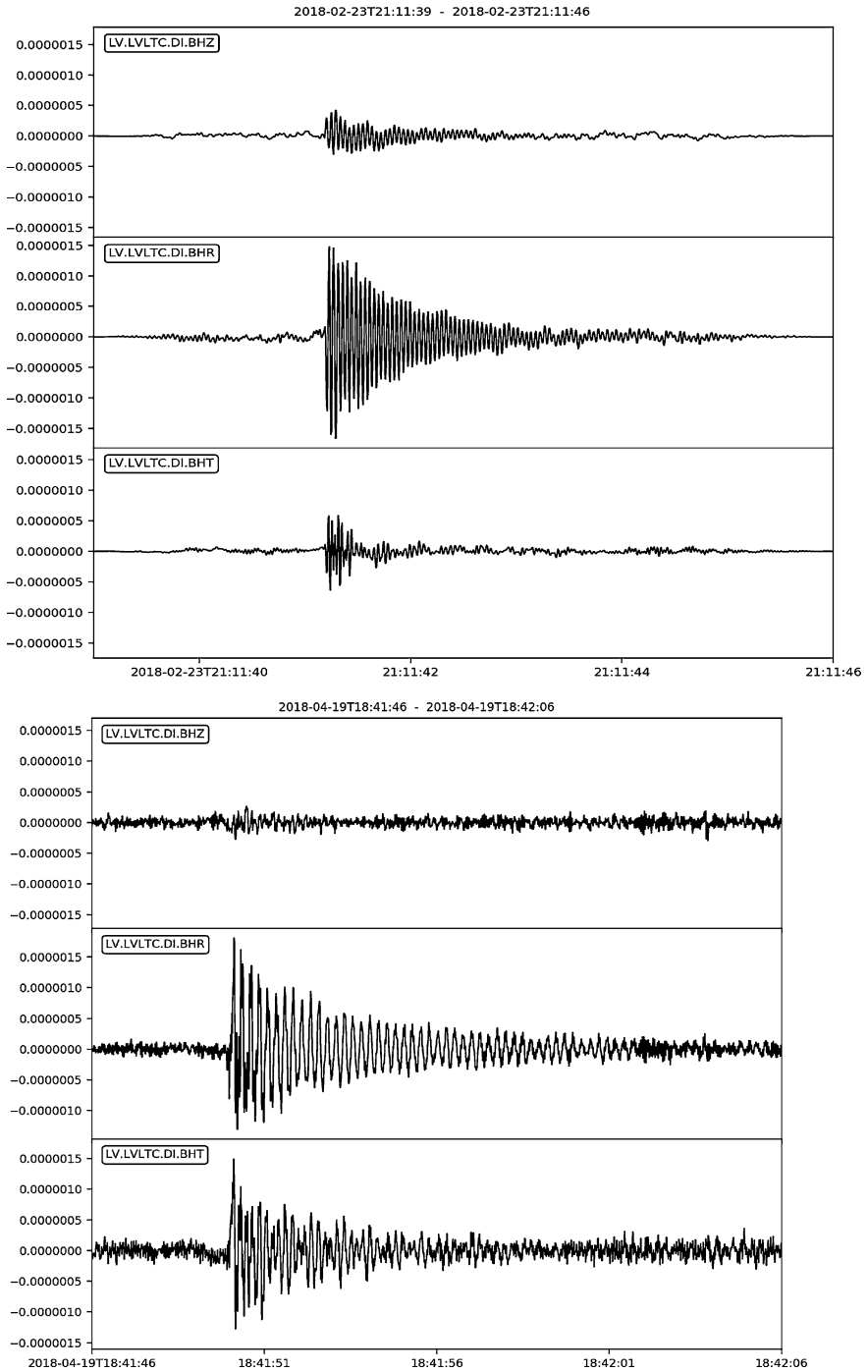


Fig. 4 Displacement seismograms for closed LSA on the left and open LSA on the right. “R” is along the tether, “T” is transverse to it, and “Z” is vertical. Note that the time scales are different: the close LSA on the left spans 7 seconds, while the open LSA on the right spans 20 seconds

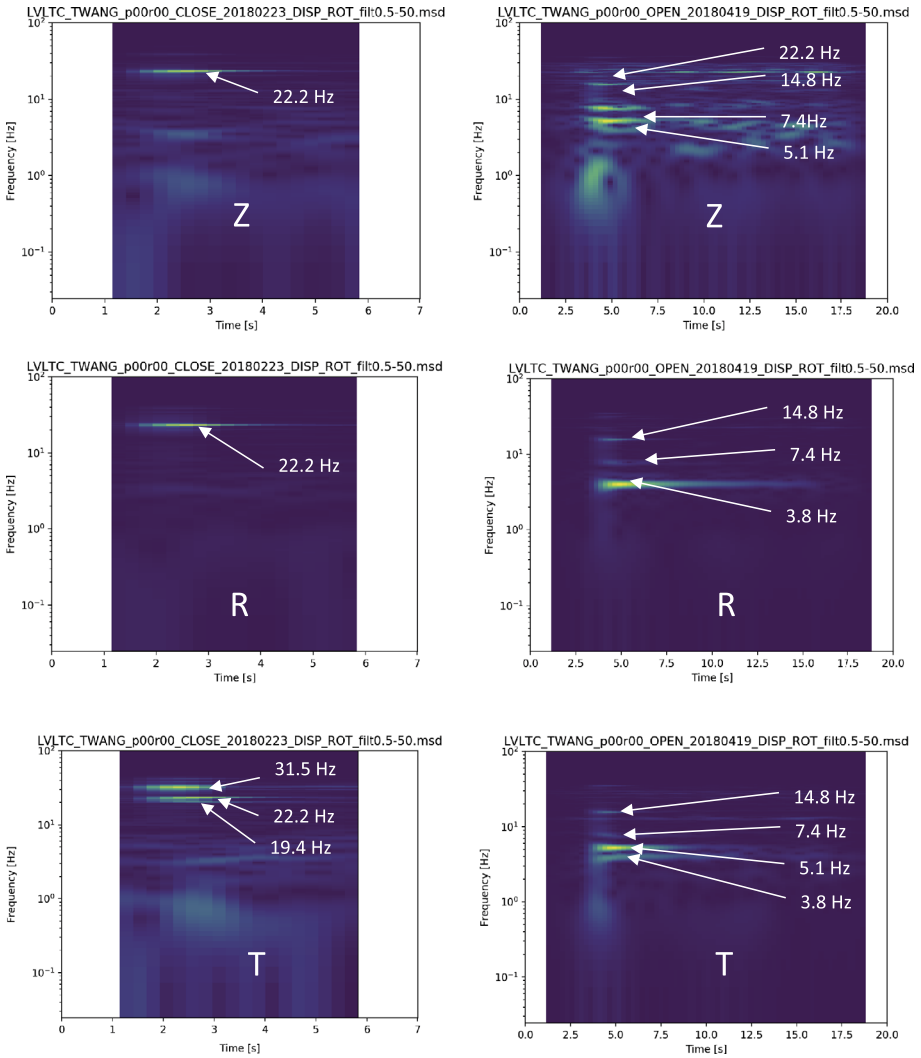


Fig. 5 Spectrograms of closed LSA (on the left) and open LSA (on the right)

being horizontal. The output of the shaker was monitored with two control sensors directly attached to the shaker’s table. The transfer function is determined by dividing the acceleration recorded at a given position on the LVL by that recorded by the control sensor. The second control sensor provides a verification of the first control sensor’s output in that a division of their spectra should lead to a flat line at unity. A close agreement between the two sensors was achieved to at least 100 Hz during both measurements.

This measurement is not used for further detailed modeling as the total system mass is much lower than that of the SEIS sensor assembly, and both the gluing of the feet to the shaker table and the extraction of all legs to a half-way position is unlike the deployment situation of SEIS. Still, it provides some first-order insights into the LVL’s resonance behavior: During acceleration in the X direction, only accelerometers pointing in that direction

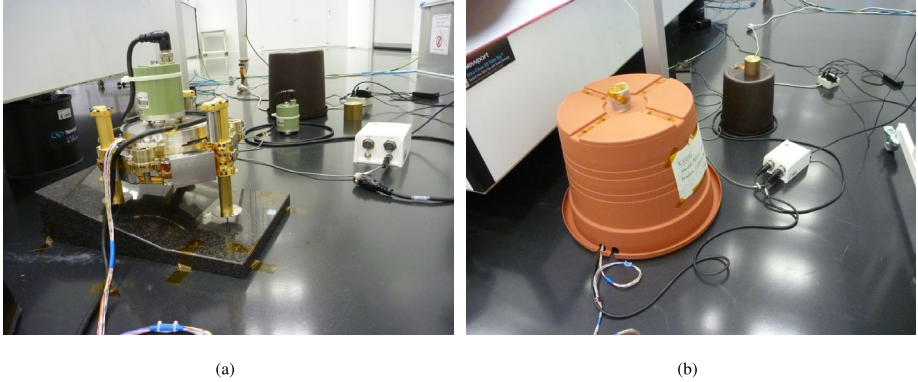


Fig. 6 LVL structure during seismic transfer function tests in the MPS clean room. (a) Setup with a Trillium compact seismometer on the metal disk at the center of the LVL structure, which is placed on a magmatic rock to simulate ground tilt. The second (“reference”) sensor is visible in the background. (b) Configuration after covering the system with weighed-down plastic buckets for actual measurement

recorded any significant signal amplification within the whole frequency band covered. The same is true for accelerations in the Y direction and accelerometers oriented the same way. The resonance peak frequencies observed for sensors at different locations on the LVL, i.e. on the hook interface, on the LVL leg, and on the damper interface, are identical in each of the two configurations, whereas the resonance amplitude varies with location. The peaks are comparatively broad, with a plateau covering about 10 Hz, and slightly shifted between X and Y directions, i.e. centered at 50 Hz vs. 48 Hz, respectively.

3.3 Seismic Transfer Function Measurements Using Ambient Noise

3.3.1 Measurement Campaign at Different Ground Tilts

We used a configuration typical in seismometer calibration to derive the seismic transfer function of the LVL FM in the lab (Holcomb 1989; Pavlis and Vernon 1994): We recorded ambient vibrations with a broad-band “test” sensor placed on the LVL and compared the data to that recorded by a “reference” sensor located on the ground close enough to assume that both sensors experience the same ground motion (Fig. 6). The sensors used are Trillium compact 120 s seismometers, connected to a six-channel 24-bit Centaur data logger (Fig. 6(a)). A metal disk was attached to the damper interface points, similar to where the VBB sphere is connected in the final SEIS setup, to provide a platform for the placement of the Trillium compact. Additional masses were also screwed to this baseplate to achieve a total mass similar to the SEIS deployed mass. The hook interface could not be connected to the LVL structure as it would have inhibited the placement of the seismometer.

The tests had to be performed in the MPS clean room. As the original Trillium compact covers are not compatible with clean room regulations, we used simple plastic buckets with a weight on top to cover the sensors and provide insulation from the air currents in the room (Fig. 6(b)). The forced venting and air-conditioning otherwise drastically increases the noise level below about 0.2 Hz.

The actual deployment conditions of the LVL are currently unknown, but the seismic transfer function strongly depends on the extracted lengths of the three linear actuators. To better understand this dependence, we determined the transfer function under a variety of

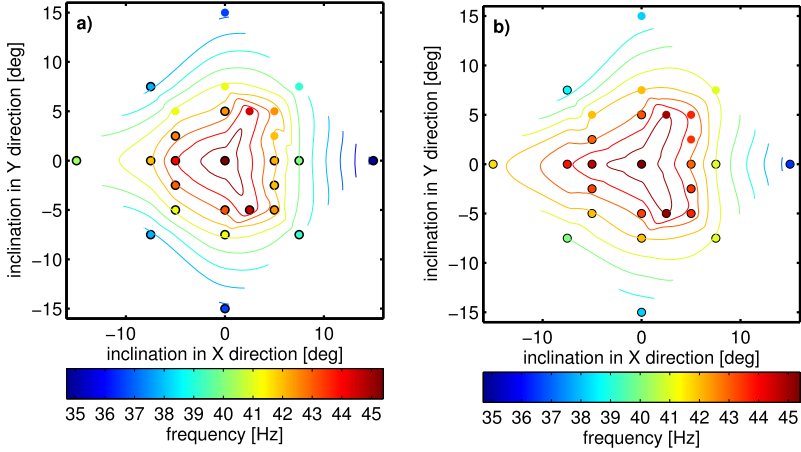


Fig. 7 Summary of LVL FM transfer function measurements at MPS. Both horizontal resonance frequencies are color-coded for a given inclination in X and Y directions, with (a) depicting the lowest resonance frequency and (b) showing the highest resonance frequency. Actual measurements were done at points circled in black; points without a black border are mirrored assuming symmetry in the Y-direction. Contour lines are based on a cubic interpolation

surface inclinations in both X and Y directions using a polished piece of magmatic rock with a slope of 15° (Fig. 6(a)). The slope covers a square area of 30×30 cm, and the flat lower edge of the rock extends over 15 cm of length at 3 cm thickness. These dimensions allow for a maximum total inclination of 15° (e.g. 15° in X-direction and 0° in Y-direction, or 7.5° in both directions simultaneously, but not 15° in both directions simultaneously). Measurements at very low angles, below 5° , are not possible with the given configuration as this would require moving the LVL more than 15 cm away from the lower edge of the slope. In addition to the measurements on the slope, we performed baseline measurements with complete retraction of all three legs at the beginning and end of the test cycle (Table 1) and one measurement at zero tilt with all legs extracted to 87.5 mm. During these measurements, the LVL was not placed on the magmatic rock, but directly on the clean room floor, which is covered by a plastic coating. This coating has been observed to deform elastically, i.e. it sinks in slightly under the weight of the LVL and recovers after the LVL has been removed.

In total, we performed measurements in 22 different configurations by leveling the LVL on the rock slope for various amounts of ground tilt between 5° and 15° and different orientations of the LVL with regard to that tilt (Fig. 7). As the LVL design is symmetrical with respect to tilts in the $\pm Y$ direction, we only conducted a limited number of measurements at the same angles in both $+Y$ and $-Y$ directions to confirm that this symmetry also appears in the resonance frequencies. The test seismometer on the LVL structure was oriented in the LVL coordinate system during each measurement, and the orientation of the reference sensor adjusted accordingly. Data were sampled at 200 Hz. Due to time constraints, the minimum duration of recordings in any configuration was only one hour of usable data. This is significantly shorter than the 10 hours of recording time suggested by Ringler et al. (2011) for instrument self-noise estimation by a similar method. However, the main interest of the measurements was the characterization of the transfer function at high frequencies (> 1 Hz), as any influence of the LVL is expected to show there, and the achieved measurement duration still allows for sufficient averaging at these frequencies. For each measurement, we

calculated the power spectral densities for the three components of the reference as well as the test sensor. The alignment of the two sensors was adjusted by minimizing the incoherent noise in the frequency domain, and the relative transfer functions calculated by division of the power spectral densities in the aligned system.

The measurements performed to check the symmetry of the system in Y-direction generally showed good agreement, i.e. less than 0.3 Hz of difference. Calculating the transfer function for each hour of data during 42 hours of continuous recording in an untilted configuration shows variations in the peak frequency in the same range, so this is within the uncertainty of the measurements themselves. We also previously performed measurements with an engineering model of the LVL in which we repeated the installation on the rock slope between measurements without driving the linear actuator legs. The observed change in measured frequencies was twice as large, $\pm 0.2\text{--}0.3$ Hz. This may indicate an additional influence of variable coupling between the feet and the ground for different installations.

In all cases where all three legs are not of equal length, there are two different resonance frequencies that, depending on configuration, either do or do not align with the X and Y axes of the system. Results are summarized in Fig. 7, which uses the symmetry in the Y -direction to predict additional data points. The three-legged structure of the LVL is readily apparent in the shape of the contour lines for both upper and lower resonance frequency. No distinct influence of the LVL on the vertical component and no clear phase effect was observed. However, deviations of the phase from zero generally occur at frequencies above 40 Hz on all three components, coinciding with a strong decrease in coherence between the signals recorded by the reference and the test sensor. For the horizontal components in particular, the phase of the estimated transfer function rapidly oscillates between $+180^\circ$ and -180° . An increased variability in the phase has also been observed by Pavlis and Vernon (1994) during seismometer calibration in cases where the coherence drops at high frequencies. Ringler et al. (2011) describe how Earth signals can become incoherent at high frequencies, even at directly adjacent sensors with well under 1 m separation, due to highly local linear and nonlinear elastic effects, which leads to a poorly determined phase estimate. We thus conclude that the unstable phase estimates at high frequencies are caused by the measurement conditions and the loss of signal coherence at high frequencies and do not reflect actual properties of the LVL's seismic transfer function.

3.3.2 Individual Measurements with a More Complete Sensor Assembly

Additional measurements of the seismic transfer function based on ambient noise were performed at CNES Toulouse during performance testing. Both the LVL FM with the test sensor on top and the reference sensor were placed on an aluminium plate and covered by a thermal and air flow protection made from polystyrene and fiber glass. All legs were extracted about half-way to an equal length and placed within metal foot wedges; the mass for this configuration was about 1350 g less than during the MPS measurements. This measurement is not representative of SEIS deployment on Mars as the aim was to level as low as possible. Additionally, the foot wedges likely influence the measurements, not only in terms of coupling to the ground, but also in terms of tether routing. However, this test allows the influence of a more complete sensor assembly to be investigated, including the bottom plate of the RWEB, the dampers, and the tether. The same horizontal resonance frequency was observed in X - and Y -directions, with no obvious influence of the tether attached to one side of the LVL on the symmetry of the system. It has to be noted, though, that the load shunt assembly (LSA) of the tether, which is supposed to decouple the mechanical vibrations of the cable from the LVL, was closed during the measurements. As observed previously, no clear LVL effects

are apparent on the vertical component and the loss of coherence between test and reference sensors leads to rapid oscillations in the phase of the transfer function above about 40 Hz.

To study the influence of regolith on the seismic transfer function, the LVL QM was set up in a sandbox, again beneath a thermal and air flow protection. Tests were done in a flat and two tilted configurations (Table 1), with a total system mass closer to the one used during the MPS campaign and the tether with open LSA attached to the LVL. Again, the LVL configurations used here do not correspond to the planned deployment configuration of SEIS, which is at the lowest possible height (i.e., with the shortest LVL legs possible), but they are the only measurements with a representative LVL on a regolith analogue material currently available. The noise level for these measurements was rather high and the coherence was not as stable as in the previous setups. Data were only sampled at 100 Hz, and no vertical resonance can be confidently identified within the highly coherent part of the measurements (0.05–25 Hz for the vertical component). No resonances of the open LSA were observed during this test, probably because it was not excited.

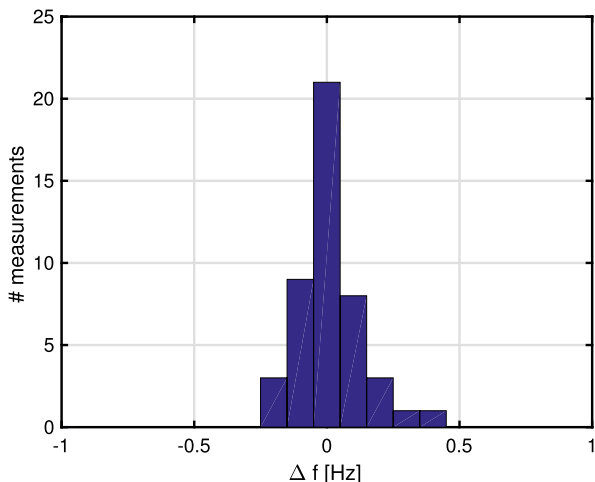
Finally, during performance tests with the integrated sensor assembly at CNES Toulouse (line number 6 in Table 1), the seismic transfer function of the LVL FM was determined using the horizontal SP sensors. As they are tuned to Martian gravity, the VBB sensors are saturated when the sensor assembly is standing on the LVL feet and is level to the ground on Earth. This does not apply to the horizontal SP sensors, though, and a dedicated measurement was done. As frequencies above 30 Hz are affected by the resonances, they are expected to be observed on the SP channels in SEIS data from Mars, too, so this is a realistic scenario. The LVL legs were again half-way extracted to equal length, which is an unlikely deployment scenario on Mars. The sensor assembly was placed on an aluminum plate and covered by the thermal and air flow protection. The tether (LSA closed), bottom panel of the RWEB, the VBB sphere, the proximity electronics boxes, and the SP boxes were attached to the LVL. The measured resonance frequencies are identical within the measurement uncertainty (Table 1) and again indicate no symmetry-breaking effect of the tether LSA in the closed configuration.

3.4 Determination of Resonances on Mars

When analyzing the data recorded by SEIS on Mars, the LVL seismic transfer function will have to be determined from ambient noise in order to both correct the data for LVL resonances, and invert the observed resonances for regolith properties with the help of the model developed below. During all of the lab tests described here, the resonance frequencies and amplitudes were determined by calculating the relative transfer function of the LVL with respect to a reference sensor placed close to the LVL. This kind of reference will not be available when SEIS is deployed on Mars. The resonances produce clearly identifiable peaks in the horizontal component power density spectra, though. We took readings of these peak frequencies for the sensor on the LVL from all 22 FM lab measurements and compared them to the resonance frequencies determined from the corresponding relative transfer functions. The frequencies obtained from the two different measurements show a close agreement, with a maximum deviation of 0.3 Hz (Fig. 8). Comparing the frequencies obtained for the SP measurement from the relative transfer function with those derived from power density spectra of the SP data gives a similar agreement. This indicates that we should be able to determine the LVL resonance frequencies with a high confidence from SEIS data recorded on Mars.

Accurately predicting the resonance amplitudes without a reference to give the background level of seismic noise will be more challenging, though. During the test measurements, amplitudes at the resonance frequencies were found to vary by an order of magnitude.

Fig. 8 Histogram of differences between the resonance frequencies obtained from the calculated transfer function and from the power density spectrum of the data recorded on the LVL. All data are from the MPS campaign with the LVL FM used



Precisely determining the amplitudes is difficult for the short-duration measurements where the gain of the transfer function shows considerable spread around the peak frequency, so longer-duration measurements are preferable. Besides, the observed amplitudes appear to depend strongly on the precise coherence between reference and test sensor around the resonance peak. Without a reference sensor, the background level of the spectrum will need to be estimated from either the horizontal components around the peak or the vertical component that does not contain the peak. However, in our lab tests, spectral amplitudes were not the same on the horizontal and vertical components. The missing reference information could lead to an underestimation of the resonance amplitudes, which might need to be adjusted iteratively when removing the resonance effects from data measured on Mars. The separation between the LVL resonances and the structural response of the Martian soil is discussed in Knapmeyer-Endrun et al. (2018).

4 Analytical Model

4.1 Construction

A simplified analytical model of the LVL structure is developed in order to predict its resonances and transfer function. The final objective being to estimate the effects of this structure on the data recorded by the VBBs and SPs on Mars. In modeling the LVL, we follow the method to detect and compensate for inconsistent coupling conditions during seismic acquisition with short-period sensors presented by Bagaini and Barajas-Olalde (2007). In their study, they analyze the coupling performances of three-component geophones, mounted on a baseplate with three spikes with a spacing of 50–65 mm. This mounting leads to resonances at frequencies of about 100 Hz for the geophones supported by the spikes. The analysis of this study is applied here to the case of the SEIS leveling system to reproduce its mechanical behavior by predicting its resonances and transfer function, and to infer the strength of coupling with the ground.

Four main elements characterize the LVL model: one platform and three legs, as depicted in Fig. 9(a). Each 3D platform-leg coupling phenomenon is modelled by one vertical spring

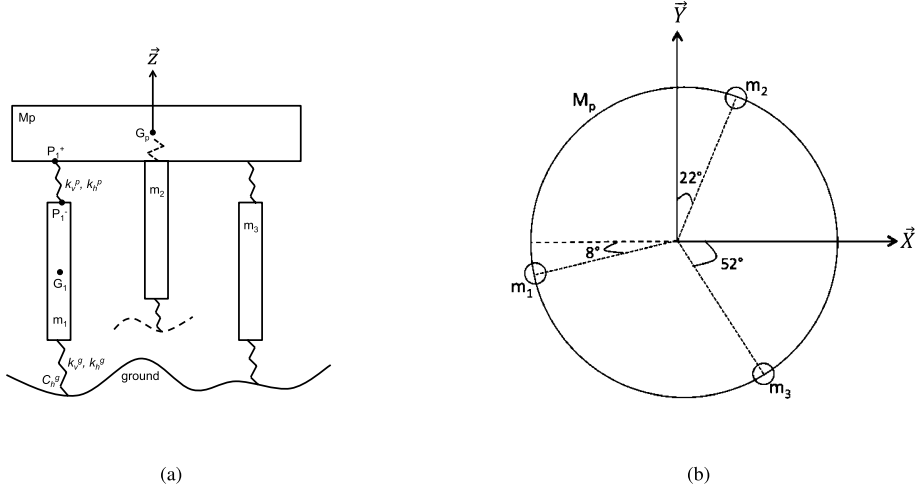


Fig. 9 A schematic view of the modeled LVL structure on which the study is based. (a) shows the LVL structure in the leg 2 direction and (b) the bottom view. The coordinate frame used is the same than in Figs. 1 and 2

Table 2 Parameters of the model as well as typical values used in the numerical applications. Question marks indicate values that are unknown for the tests reported here as well as for the deployment on Mars and need to be derived from the observed resonances. Note that M_p is not an adjustable parameter and is deduced from M_{tot} and m_i values

Parameter	Description	Value	Unit
M_{tot}	Total mass	9.082	kg
m_i	Legs mass	0.052–0.098	kg
J_{tot}	Total moment of inertia matrix	0.237 -0.012 -0.002 -0.012 0.244 -0.001 -0.002 -0.001 0.108	kg m ²
k_v^p	Platform-leg vertical spring constants	3.3×10^6	N/m
k_h^p	Platform-leg horizontal spring constants	$4-12.5 \times 10^5$	N/m
k_v^g	Leg-ground vertical spring constants	?	N/m
k_h^g	Leg-ground horizontal spring constants	?	N/m
C_h^g	Ground torque induced on the legs	?	N m/rad

with a rigidity constant k_v^p , and two horizontal ones with a representative constant k_h^p . Likewise, each 3D foot-ground coupling phenomenon is described by constants k_v^g and k_h^g . All of these rigidity constants are associated to design requirements. Equivalent masses for the platform subsystem M_p and the three legs m_1, m_2 and m_3 are used to complete the system. This configuration permits six degrees of freedom for each subsystem. However, as the complete instrument configuration does not allow for a rotation of the legs around the vertical axis, the final system has, in total, 12 degrees of freedom in translation and 9 in rotation. The infinitesimal oscillating rotation of the LVL around the Z axis around the reference position can however be made mostly through the deformations of the three contact points. All parameters of the model, including their values are listed in Table 2.

Newton's second law is applied for each subsystem of the global structure in both translation and rotation. For the LVL platform this gives:

$$M_p \frac{d^2}{dt^2} \overrightarrow{\Delta G_p} = \sum_{i=1}^3 \overrightarrow{\Delta F_i^+}, \quad (1)$$

where M_p represents the mass of the platform and the second derivative term is the platform's center of mass acceleration in translation. Here and in the next equations, Δ is used for all forces and positions measured with respect to the reference position of the SEIS instrument. This also explains why neither weight nor ground reaction in the equilibrium state appear in these equations. Finally, the term $\overrightarrow{\Delta F_i^+}$ is the force linked to the relative displacement between the two ends P_i^+ and P_i^- of the spring which is placed on top of the leg i , given by:

$$\overrightarrow{\Delta F_i^+} = -k^p (\overrightarrow{\Delta P_i^+} - \overrightarrow{\Delta P_i^-}), \quad (2)$$

where k^p corresponds to the platform-leg spring constant. Knowing that the platform is a non-deformable solid, the displacement of point P_i^+ can be defined as

$$\overrightarrow{\Delta P_i^+} = \overrightarrow{\Delta G_p} + \overrightarrow{\Omega_p} \times \overrightarrow{G_p P_i^+}, \quad (3)$$

$\overrightarrow{\Omega_p}$ represents the platform rotation, the symbol \times is the curl product and $\overrightarrow{G_p P_i^+}$ corresponds to the vector between the platform's center of mass and the top of the considered spring. The same definition is used for the expression of the displacement of point P_i^- . Next, Newton's second law is also written for the translation of each leg:

$$m_i \frac{d^2}{dt^2} \overrightarrow{\Delta G_i} = -\overrightarrow{\Delta F_i^+} + \overrightarrow{\Delta F_i^S}. \quad (4)$$

The second derivative term in (4) represents the considered leg's center of mass acceleration in translation and m_i is the mass of the considered leg's. The force linked to the relative displacement between the two end points of the bottom spring S_i^+ and S_i^- , $\overrightarrow{\Delta F_i^S}$, can be expressed as:

$$\overrightarrow{\Delta F_i^S} = -k^g (\overrightarrow{\Delta S_i^+} - \overrightarrow{\Delta S_i^-}), \quad (5)$$

where k^g corresponds to the leg-ground spring constant. The term $\overrightarrow{\Delta S_i^-}$ is equal to zero because this point is on the ground, and as in Eq. (3) the displacement of S_i^+ is given by:

$$\overrightarrow{\Delta S_i^+} = \overrightarrow{\Delta G_i} + \overrightarrow{\Omega_i} \times \overrightarrow{G_i S_i^+}, \quad (6)$$

where $\overrightarrow{\Omega_i}$ represents the rotation of the considered leg and $\overrightarrow{G_i S_i^+}$ corresponds to the vector between the considered leg's center of mass and the top of the considered spring on the ground. However, each of the elastic links is not isotropic. However, the elastic contacts with ground are not assumed to be isotropic. We therefore model them with two different stiffness constants for the springs: one for the vertical and a second for the horizontal. Considering this new information and knowing that only the leg tilts are considered (i.e. no rotation

around the vertical axis), ΔF_i^+ can be corrected:

$$\begin{aligned} \overrightarrow{\Delta F_i^+} &= -k_h^p (\overrightarrow{\Delta G_p} + \overrightarrow{\mathcal{O}_2} \times \overrightarrow{G_p P_i^+} - \overrightarrow{\Delta G_i} - \overrightarrow{\mathcal{O}_2} \times \overrightarrow{G_i P_i^-}) \\ &\quad - (k_v^p - k_h^p) (\overrightarrow{\Delta G_p} \cdot \vec{n} + \overrightarrow{\mathcal{O}_2} \times \overrightarrow{G_p P_i^+} \cdot \vec{n} - \overrightarrow{\Delta G_i} \cdot \vec{n}) \cdot \vec{n}, \end{aligned} \quad (7)$$

where the symbol \cdot corresponds to the scalar product. The different stiffness constants are detailed in Table 2 and \vec{n} is the unit vector in the vertical direction. In the same way, ΔF_i^S is corrected. Twelve translation equations are finally written: three equations for the platform and three for each leg of the LVL structure. Then, the platform rotation is defined as:

$$[J_p] \frac{d^2}{dt^2} \overrightarrow{\mathcal{O}_2} = \overrightarrow{G_p P_1^+} \times \overrightarrow{\Delta F_1^+} + \overrightarrow{G_p P_2^+} \times \overrightarrow{\Delta F_2^+} + \overrightarrow{G_p P_3^+} \times \overrightarrow{\Delta F_3^+}, \quad (8)$$

where $[J_p]$ represents the platform's moment of inertia matrix, the second derivative term is the platform's center of mass rotation. Then, the leg rotations are defined in the same way:

$$[J_i] \frac{d^2}{dt^2} \overrightarrow{\mathcal{O}_i} = -\overrightarrow{G_i P_i^-} \times \overrightarrow{\Delta F_i^+} + \overrightarrow{G_i S_i^+} \times \overrightarrow{\Delta F_i^S}, \quad (9)$$

where $[J_i]$ represents the moment inertia matrix of the feet, and the following expression for the restoring torque (on the feet) when the rotation is perpendicular to \vec{n} :

$$\overrightarrow{G_i S_i^+} \times \overrightarrow{\Delta F_i^+} = \vec{C}_i = -C_h^s (\overrightarrow{\mathcal{O}_i} - (\overrightarrow{\mathcal{O}_i} \cdot \vec{n}) \vec{n}). \quad (10)$$

Like for the platform, every term is written in the associated leg's frame. Finally, three equations are written to define the platform rotation, and two for each leg's rotation, because a rotation of the legs around the vertical axis is not possible. To compute the LVL response by using the model, different inertias must be defined. The total inertia is known from the overall SEIS model and delivered hardware, and inertias of the legs can be found by using their characteristics. Indeed, it is known that:

$$[J_{leg_i/platform}] = [J_{leg_i/CG}] - [J_{onlyleg}] \quad (11)$$

where $[J_{leg_i/platform}]$ is the inertia of the leg i in the platform's frame and the term $[J_{leg_i/CG}]$ represents the inertia of the leg i relative to the leg's center of mass which can be expressed as:

$$\begin{bmatrix} 4m_i(Y_i^2 + Z_i^2) & -4m_i Y_i Z_i & -4m_i Z_i X_i \\ -4m_i X_i Y_i & 4m_i(X_i^2 + Z_i^2) & -4m_i Z_i Y_i \\ -4m_i X_i Z_i & -4m_i Y_i Z_i & 4m_i(X_i^2 + Y_i^2) \end{bmatrix}, \quad (12)$$

where X_i , Y_i and Z_i are the coordinates of the considered foot's center of mass. A leg inertia $[J_{onlyleg}]$ is expressed as:

$$\begin{bmatrix} \frac{1}{4}m_i r^2 + \frac{2}{3}m_i H^2 & 0 & 0 \\ 0 & \frac{1}{4}m_i r^2 + \frac{2}{3}m_i H^2 & 0 \\ 0 & 0 & \frac{1}{2}m_i r^2 \end{bmatrix}. \quad (13)$$

The terms H and r are the corresponding leg's height and radius, respectively. Finally, the platform's inertia can be defined as the total moment of inertia less the sum of the 3 legs' moments of inertia (Eq. (11)).

Combining all equations, the mass (which includes also the moment of inertia matrices) and rigidity matrices, $[M]$ and $[K]$, respectively (both size 21×21), are defined and implemented numerically. This allows the eigenmodes of the global structure to be found. The adjustable parameters in the model are the various masses, the length of each leg, the stiffness of the springs and the torque induced by the ground on the legs C_h^g . Once the extracted lengths of the LVL legs are known, this also sets their masses and the horizontal stiffness k_h^p between them and the platform thanks to their mechanical characteristics. Values for k_h^p and k_v^g can be selected arbitrarily as some numerical simulations show that they do not significantly influence the results. The main parameters to adjust because of their considerable influence on the calculated resonances, are k_h^g and C_h^g .

We perform two last modifications in our model and associated equations: although the center of mass of the total assembly (noted CoG) is close from the center of mass of the platform, slight movements are expected due to the slight non-rigidity of the feet-to-platform links. We therefore first consider the center of gravity of the assembly as coordinate origin and express both the platform and feet positions with respect to the SEIS center of mass. Secondly, we do have attenuation processes in the ground deformation. We introduce an attenuation quality coefficient Q of the elastic forces against the ground in the resonance determination. This parameter is also adjustable in the model. It allows the eigenresonance amplitudes in the transfer function to be changed. The LVL response $[R]$ is then calculated with the matlab “eig” function which solves the problem of eigen values:

$$[R] = [P]^{-1}([K] - [M] \cdot [\Omega^2])^{-1} \cdot [P][D], \quad (14)$$

where $[P]$ is the transfer matrix toward the eigenvector base, $[\Omega]$ corresponds to the eigenvalue matrix, and $[D]$ represents the three vectors of ground displacement applied to the three feet in contact with the ground (ΔS_i^+). This response can then be used to compute either the 3D velocity translation and rotation rate of the LVL generated by the feet displacement, or the acceleration measured by the six axis sensors on their mounting locations on the LVL, and therefore the transfer function of SEIS with respect to ground displacement or ground acceleration.

4.2 Validation

Eigenmodes are determined with a matlab software that we have developed by coding the matrices. A verification process is performed step by step, gradually increasing the complexity of motions of the system, namely releasing at each new step one more degree of freedom. Results of all steps are represented in Fig. 10. First, a translation-only configuration is chosen; rotation is not modeled. To begin, all stiffnesses are considered infinite except k_h^g , which is zero. Under these conditions one would expect to find two orthogonal modes at $f = 0$ Hz corresponding to horizontal displacement of the center of gravity. These two modes of the platform’s translation along the x and y axes are also found in the numerical solution (Fig. 10(a)). One additional mode appears at less than infinite frequency (smaller than 5×10^5 Hz), caused by the parallel springs.

The second step of the validation process consists of releasing the vertical motion between the ground and the feet, so that $k_v^g = 10^6$ N/m. One vertical mode must be found at:

$$\omega = \sqrt{\frac{3 \cdot k}{M}}, \quad (15)$$

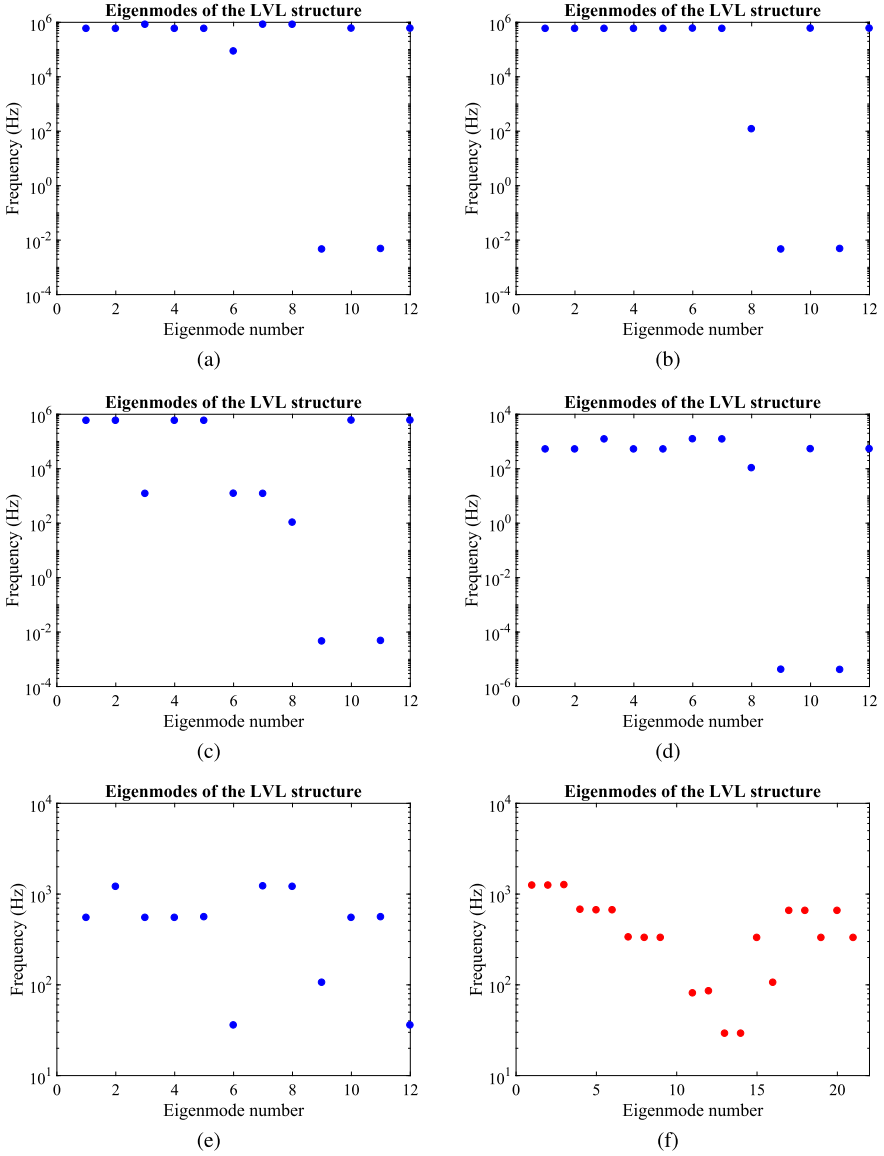


Fig. 10 (a) to (e) are the results of the first five steps of model validation, only for translation, showing all the frequencies of the determined twelve eigenmodes. (f) represents the same configuration with rotation movements added

which induces:

$$f = \frac{1}{2 \cdot \pi} \cdot \sqrt{\frac{3 \cdot k}{M}}, \quad (16)$$

where M is the total mass of the LVL and is equal to 5.3 kg in this example, resulting in $f = 119.7$ Hz. Figure 10(b) shows this mode well (number 8), and a glance at the eigenvector indicates that it is a vertical downward translation of the platform.

Next, the vertical displacement between feet and the platform is released, putting k_y^p at its minimum value. This time, the old vertical mode must match with a configuration of two springs in series, thus with a lower frequency than before: $f = 104.9$ Hz. This frequency is readily observed in Fig. 10(c) (mode number 8). Moreover, we also observe the frequency decrease of three modes (modes number 3, 6 and 7) which appears with the release of the complete vertical stiffness of the system. They correspond to vertical translations of the different feet.

The fourth step of the validation consists in releasing k_h^p , considering a mean extraction of feet, namely $k_h^p = 7.9 \times 10^5$ N/m which stems from the mechanical properties of the LVL's legs and is determined by their length. All high frequencies which correspond to translations of the feet in $\pm X$ and $\pm Y$ direction decrease (Fig. 10(d)). This is due to a lower horizontal rigidity of the structure.

Finally, k_h^g is set to 10^5 N/m, which means that horizontal translation is more constrained. Thus, Fig. 10(e) shows the disappearance of the $f = 0$ Hz modes. This is a configuration for a structure embedded in the martian ground, i.e. feet cones penetrating the regolith. Indeed, for the first four steps of the validation process, k_h^g was zero, which means that the structure could translate horizontally freely on the ground. This is not possible anymore with the current setting of k_h^g , and the $f = 0$ Hz modes can not exist.

The next step consists in looking at this model with rotational motions added. The twelve first modes correspond well to the translation modes observed in the previous step, but they are mixed. This means that, when using identical parameters but adding the rotation equations into the model, we find the same translation modes, but not positioned at the same mode numbers, and neither with exactly the same frequencies. A closer look at each found rotational mode informs us on their coherence with our modeled LVL structure.

Figure 11 shows an example of these first results of the model. The figures show all the LVL's vibration modes: resonances in (a), and all the structure's mode displacements (b) and (c). The two horizontal modes observed in Fig. 11 have a frequency within the range covered by the measurements previously detailed. Indeed, the seismic transfer function measurements made on the shaker and during the tests using ambient noise listed in Table 1 also reported two vibration modes in translation of the upper part of the LVL structure. This good agreement with the laboratory results is a first indication that the model is indeed reproducing the correct behavior.

A further validation of the model was done by only changing the mass of the platform or the leg lengths (same length for all three legs). When either of these parameters increases, the horizontal frequencies decrease (see Fig. 12). The same evolution is observed in all of the different tests performed in laboratories and listed in Table 1. However, we cannot add their resonance values to our figures and compare them to our simulations. Indeed, the only way to find exactly the same resonances values is to change k_h^g and C_h^g in the code, which means that the different leg lengths induce different coupling conditions between the feet and the ground in a real configuration, which are not quantified. Moreover, no measurements with different masses and exactly the same leg lengths are available for the LVL QM or FM.

The model can also describe the complete LVL transfer function as determined during test measurements in the laboratory. Figure 13 shows an example for the baseline configuration (lowest LVL height, with all legs at the same length) for which the measurements correspond to the first case of Table 1. The superposition of both curves confirms that the model can faithfully predict the real LVL behavior. This is also observed in Fig. 14. This curve shows the LVL transfer function in a tilted configuration on sand (fifth experiment of Table 1), which can also be explained by the model. Finally, the last laboratory measurement which was realized on the LVL FM (number 6 in Table 1) with the two horizontal SP sensors is also reproduced well by the modeled transfer function (Fig. 15).

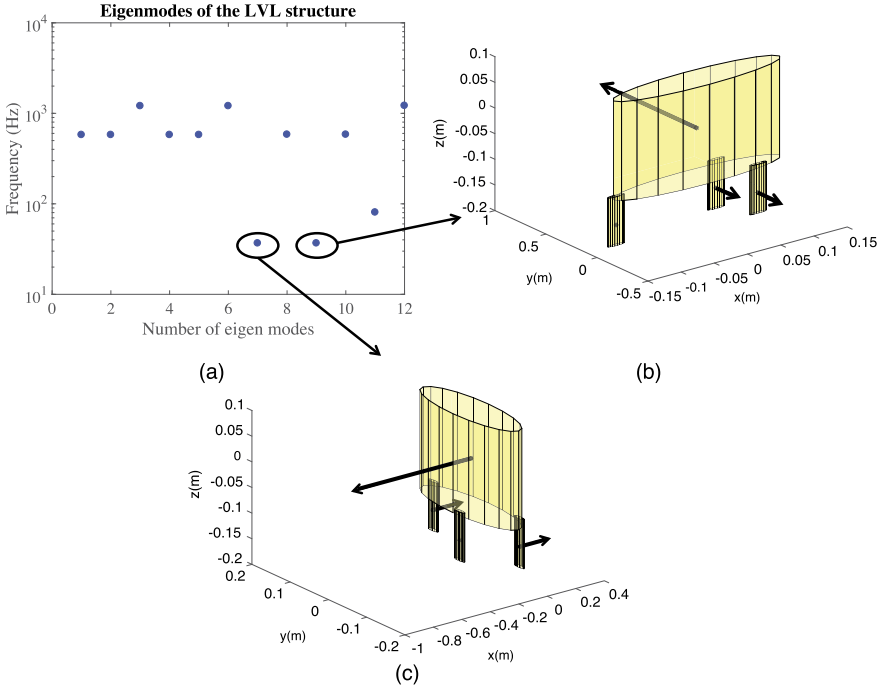


Fig. 11 Model results including both translational and rotational motion of the LVL. (a) Resonance frequencies of all 21 modes. (b) Horizontal translation mode (mode number 14) of the platform along the x-axis. (c) Horizontal translation mode (mode number 7) of the platform along the y-axis. The arrows give the direction of the considered center of mass' motion

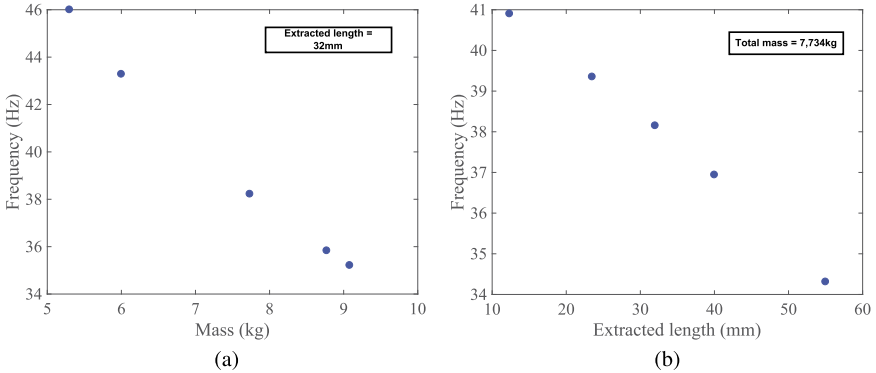


Fig. 12 Frequency of the horizontal translation modes of the LVL platform found with the model as a function of the mass (a) or the legs length (b), without a change of any other parameters ($k_v^p = 3.3 \times 10^6$ N/m, $k_v^g = 1 \times 10^6$ N/m, $k_h^g = 3 \times 10^5$ N/m and $C_h^g = 5.73 \times 10^3$ N m)

5 Application

The translation part of the model was verified by considering an embedded structure, progressively released, and the rotation modes were then found to be consistent. The two hori-

Fig. 13 Measured (in blue) and modeled (in red) gain of the horizontal transfer functions on x-axis (top curve) and y-axis (bottom curve) in the LVL FM baseline configuration (all legs extracted by 0.5 mm). This test corresponds to the first one in Table 1. Masses, extracted lengths of the legs, and k_h^p values were set to those of the measurement configuration, whereas the other parameters were adjusted to fit the data: $Q = 33$, $k_h^s = 3.15 \times 10^5$ N/m and $C_h^s = 3.7 \times 10^4$ N m/rad

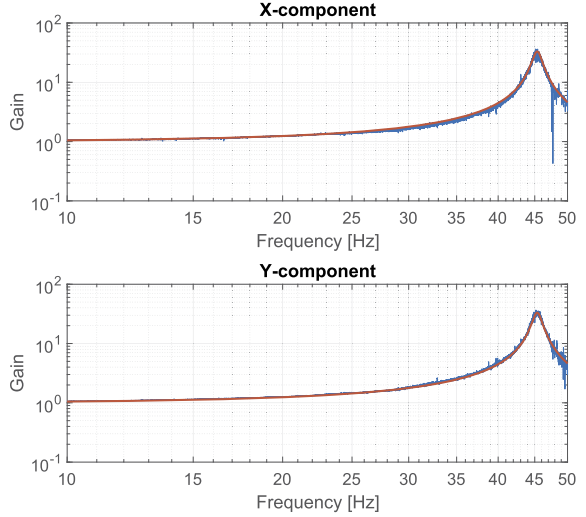
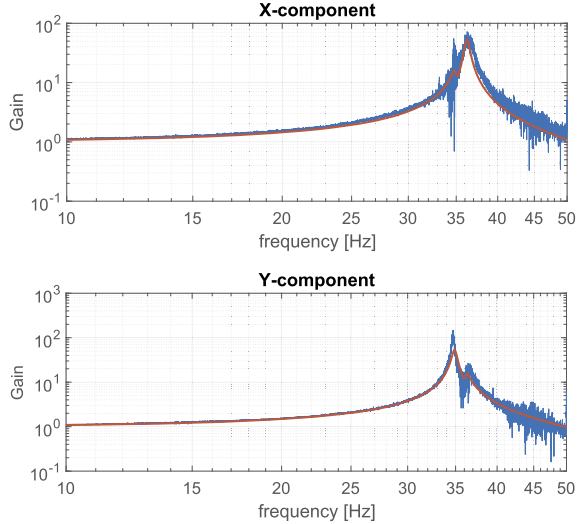


Fig. 14 Measured (in blue) and modeled (in red) gain of the horizontal transfer functions on x-axis (top curve) and y-axis (bottom curve) in one 15° tilted configuration of the LVL QM on sand (test number 5 in Table 1). Masses, extracted lengths of the legs, and k_h^p values were set to those of the measurement configuration, whereas the other parameters were adjusted to fit the data: $Q = 60$,
 $k_h^s 1 = 1.3 \times 10^5$ N/m,
 $k_h^s 2 = 6.1 \times 10^5$ N/m,
 $k_h^s 3 = 0.63 \times 10^5$ N/m,
 $C_h^s 1 = 6.88 \times 10^4$ N m/rad,
 $C_h^s 2 = 6.3 \times 10^4$ N m/rad and
 $C_h^s 3 = 1.1 \times 10^4$ N m/rad

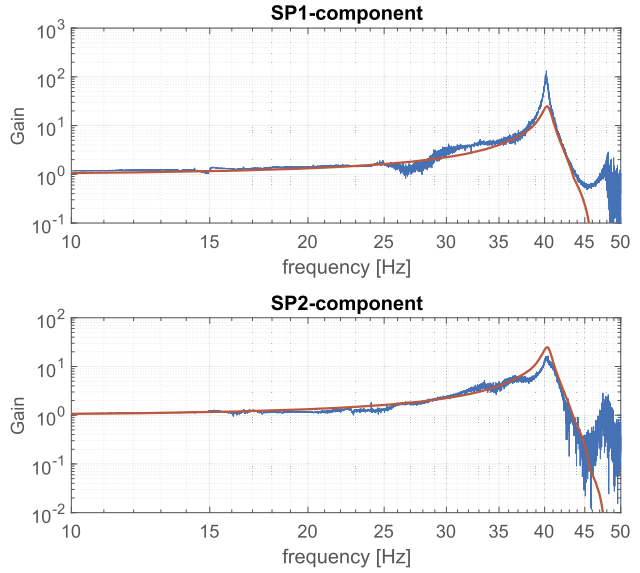


zontal translation modes of the platform, always observed between 35 and 50 Hz in both the model results and the laboratory measurements, give evidence of the model's fidelity to reality. In addition, the same evolution of eigenfrequencies with mass and leg lengths between the measured and modeled resonances is a further indication that this model can be used to estimate the LVL's mechanical modes. Finally, the transfer function similarity between the real measurements and this numerical model guarantees that it can be used to study the seismic response of SEIS on Mars in the future.

5.1 LVL Resonance on Mars

One obvious application of this model is to predict resonances of the LVL which could affect SEIS measurements and inversely, from the observed resonances, to constrain the properties

Fig. 15 Measured (in blue) and modeled (in red) gain of the transfer functions of the two horizontal short period sensors on the LVL FM: SP1 (top curve) and SP2 (bottom curve), corresponding to the sensor locations given in Fig. 2. Masses, extracted lengths of the legs, and k_h^p values were set to those of the measurement configuration, whereas the other parameters were adjusted to fit the data: $Q = 40$, all $k_h^g = 2.9 \times 10^5$ N/m and all $C_h^g = 1.72 \times 10^4$ N m/rad



of the ground. With a sampling rate of 100 Hz, the Nyquist frequency of the SEIS sensors in nominal operations is 50 Hz. By using a combination of the nominal antialiasing FIR filter for the VBBs passing information between 0 to 50 Hz and a bandpass filter passing information between 50 Hz and 100 Hz for the SP sensors, the bandwidth of the combined VBBs and SPs data can be extended to 100 Hz (Schmelzbach et al. 2018, in preparation). This means that resonances below these frequencies will be seen on the seismic signal of the instrument and could disturb SEIS measurements. Depending on the adjustable parameter values, sometimes the results can give 50 to 100 Hz resonances. But the major way in which the LVL affects the records is by horizontal resonances of the system due to the details of the leg structure. These resonances were first observed during the test of the LVL structure on a shaker. During a more thorough investigation of the LVL's seismic transfer functions using ambient noise, horizontal resonance frequencies were located between 34.7 and 46.4 Hz, depending on the LVL configuration. When calculating all of the 21 LVL vibration modes (resonances and displacements of the structure) with the analytical model, only two of the obtained frequencies are below 50 Hz. Figure 11 shows that they also correspond to horizontal translations of the platform in X- and Y-directions, respectively, which is in good agreement with the laboratory results.

The model also indicates that the horizontal resonance frequencies of the LVL are highly dependent on ground properties. Indeed, when the masses and the leg lengths are set (and therefore also k_h^p because of its dependance on the extracted length of the legs), the parameter space of the other rigidity constants can be explored: the vertical and horizontal elastic stiffness between the feet and the ground k_v^g and k_h^g , and the torque induced on the feet by the ground C_h^g . Note that the value of the vertical stiffness between the platform and the legs k_v^p is provided by the engineering team: at 3.3×10^6 N/m. By changing only one of the other model parameters per simulation, it is shown that only two of them can significantly change the horizontal resonance frequencies: k_h^g and C_h^g . For example, if k_v^g increases by six orders of magnitude, neither of the horizontal resonance frequencies are impacted, whereas an increase in k_h^g or C_h^g considerably increases the frequency values. This is shown in Fig. 16.

Fig. 16 Sensitivity of the LVL resonance frequencies to the values of the elastic stiffness of the ground material in contact with the LVL's feet (k_h^g (in blue) and k_v^g (in red), both in N/m and related to horizontal and vertical forces, respectively), and the torque C_h^g (in green) in N m/rad, with respect to a rotation perpendicular to the foot direction

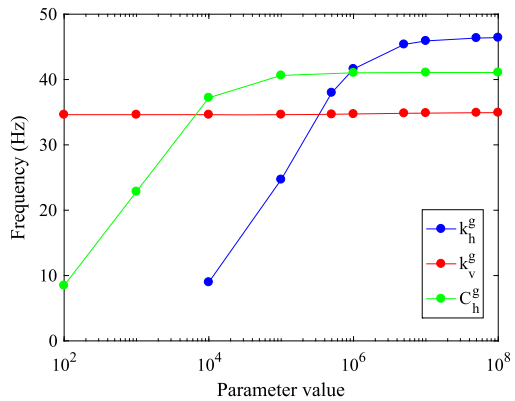
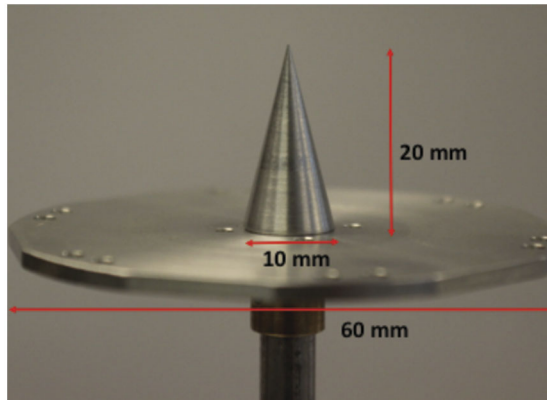


Fig. 17 Design of the SEIS foot, composed of a cone (10 mm diameter, 20 mm length) fixed on a 60 mm disk



5.1.1 Resonances Prediction from Laboratory Analog Measurements

The laboratory investigation of the interaction between one SEIS foot and possible Martian regolith simulants was carried out by using a specifically developed system, in which a replica of the SEIS foot was slowly penetrated into a mass of Martian regolith simulant of controlled density under the self-weight supported by one of the three SEIS feet. Properties of the Martian regolith simulant are described in Delage et al. (2017).

Once the foot had penetrated the regolith, cyclic loading at small strain were carefully conducted so as to identify the elastic interaction between the foot and the simulant. The detailed shape of the SEIS foot is presented in Fig. 17. It is composed of a 60 mm diameter disk on which a cone is fixed. The shape of the cone was designed by carrying out penetration tests to make sure that full penetration would be reached under the SEIS self-weight under Mars gravity. This resulted in designing a 20 mm long cone with 10 mm maximum diameter (Delage et al. 2017).

Figure 18(a) shows the device used to investigate the foot/simulant interaction. As seen in the figure, a cylindrical container (239 mm diameter, 108 mm height) full of a Martian regolith simulant called Mojave simulant, placed at controlled density, is put on the pedestal of a triaxial press, that can be slowly moved upwards. This simulant, provided by JPL, is a mix of MMS simulant (Peters et al. 2008) with some natural Mojave sand from the same area. Its characteristics and mechanical properties have been investigated by Delage et al.

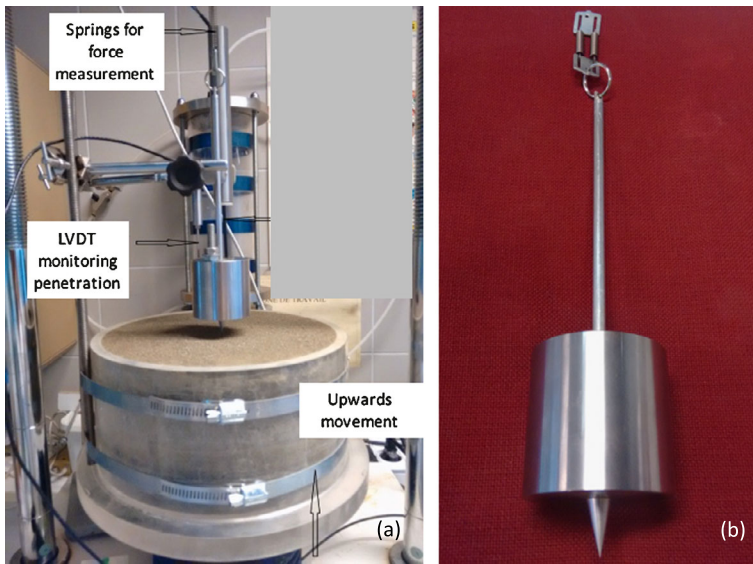


Fig. 18 (a) Testing device with the container full of Martian Mojave sand regolith at controlled density. The container is placed on the pedestal of a triaxial press and slowly driven up at a controlled upwards speed. Once the tip of the cone comes in contact with the soil, penetration starts and the corresponding force resulting from the cone/soil interaction is monitored by the change in length of the spring. (b) SEIS foot fixed at the bottom of a steel cylindrical mass corresponding to the weight supported by one of the three SEIS feet under Mars gravity (1 kg). The diameter of the plate is 60 mm. The upper diameter of the cone is 10 mm and its height is 20 mm. One can see the pair of springs used to suspend the mass. The force resulting from the contact between the cone and the soil during penetration and elastic loading tests is monitored by measuring the changes in length of the calibrated spring by means of a LVDT (Linear Variable Differential Transformer) displacement measuring device

(2017). The medium D50 diameter of the simulant is equal to 300 μm . As seen in Fig. 18(b), the SEIS foot shown in Fig. 17 is fixed to a 1 kg cylindrical steel mass corresponding to the average weight supported by one of the three SEIS feet under Mars' gravity. The photo also shows the two calibrated springs used to suspend the foot and mass to the bracket of a triaxial press, as seen in Fig. 18(b). Measuring the changes in the springs' length thanks to a LVDT (Linear Variable Differential Transformer) provides the force resulting from the penetration of the cone into the simulant. Penetration is made possible by gently moving the pedestal of the press upwards. In other words, the springs initially support the whole suspended mass, that is progressively released during cone penetration by the increasing upwards axial vertical force supported by the simulant. Another LVDT sensor provides the change in axial penetration with time, allowing the penetration curve to be monitored in terms of changes in force with respect to penetration depth. Once the cone is fully penetrated and the disk is in contact with the simulant, one can then measure the axial elastic constant characterizing the axial simulant/foot elastic interaction, by applying small upwards and downwards movements to the pedestal. Some tests were performed on a soil specimen prepared at a controlled density of 1640 kg/m^3 . To do so, the simulant was placed in the container by pouring successive 30 mm thick layers, that were carefully compacted to the required density by using a tamping system shown in Fig. 19. To determine the elastic axial response once full cone penetration under the self-weight supported by the SEIS foot is reached, the axial force was slowly cycled between its maximal value (10 N) and a minimal value of 8 N. As seen in

Fig. 19 Tamping procedure to obtain the required density

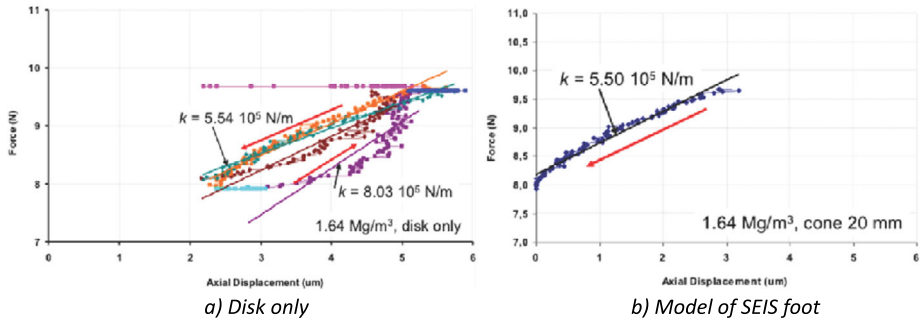
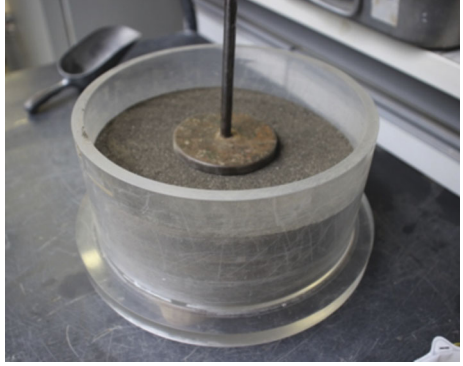
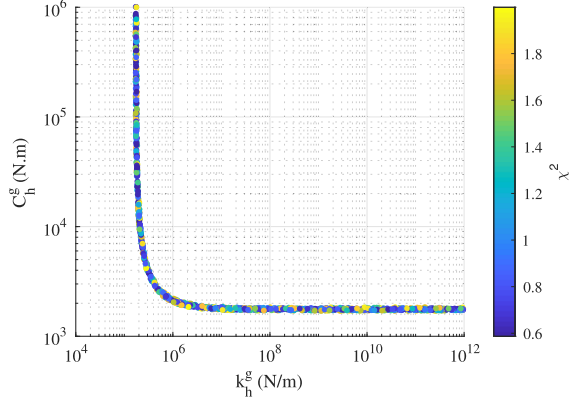


Fig. 20 Determination of the elastic axial constant between a specimen of Mars Mojave simulant compacted at a density of 1640 kg/m^3 and a 60 mm diameter plate (a) and a model of the SEIS foot with the 10 mm diameter and 20 mm high cone (b). The axial force is cycled between 10 and 8 N and the resulting displacements are in the $3 \mu\text{m}$ range, close to the resolution limit of the LVDT system. The successive tests carried out with the disk only provide a constant between 5.54×10^5 and $8.03 \times 10^5 \text{ N/m}$ whereas the test run for the full SEIS foot (with cone) found a value of $5.50 \times 10^5 \text{ N/m}$, showing a negligible effect of the cone

Fig. 20, the values obtained with a simulant density of 1640 kg/m^3 are between 5.54×10^5 and $8.03 \times 10^5 \text{ N/m}$, from successive loading cycles carried out with the disk only. The unloading path from 10 down to 8 N carried out with the model of SEIS foot provides a value of $5.5 \times 10^5 \text{ N/m}$, showing little effect of the cone. Note that the displacement involved in the tests are rather within the range of $3 \mu\text{m}$, not far from the accuracy limit of the LVDT used. The horizontal stiffness has not yet been determined by laboratory measurements. The link between the parameters k_h^g and C_h^g and the elastic ground properties (Poisson's ratio ν and Young's modulus E) can however be expressed analytically for the case of a simple circular plate of radius a on a semi-infinite elastic mass as follows (Poulos and Davis 1974):

$$\begin{aligned}
 k_h^g &= \frac{16(1-\nu)Ea}{(7-8\nu)(1+\nu)}, \\
 C_h^g &= \frac{4Ea^3}{3(1-\nu^2)}, \\
 \frac{k_h^g}{C_h^g} &= \frac{12(1-\nu)^2}{(7-8\nu)a^2}.
 \end{aligned} \tag{17}$$

Fig. 21 C_h^g as a function of k_h^g and χ^2 for the case number 3 of Table 1



For $a = 3$ cm and $\nu = 0.22$, this leads to a ratio of about 1548 rad/m^2 . The spikes will likely increase this ratio further and this suggests that the resonance frequencies will therefore be most sensitive to C_h^g . For a density ranging from 1300 to 1500 kg/m^3 and a shear wave velocity between 110 and 164 m/s , which results in having the Young modulus E comprised between 13.8 and 35.3 MPa , the values found for the horizontal stiffness k_h^g are between 8×10^5 and $2 \times 10^6 \text{ N/m}$. With the uncertainty on the ν value, this is in good agreement with the Figs. 13, 14 and 15. The calculated C_h^g values are comprised between 5×10^2 and $1.4 \times 10^3 \text{ N m/rad}$ which is smaller than the model values but the elastic solutions of Poulos and Davis (1974) don't take into account the fact that the sand is loaded by the weight of SEIS which can increase the Young modulus below the LVL feet. Moreover these formula only consider a disk and not our foot design with a spike, that may also have some influence on the soil response.

5.1.2 Inversion Perspectives

When the resonance frequency will be measured, an inversion of its value will be possible with the goal to better constrain the ground properties. In order to test such future work with Mars observations, an inversion test has been made, but using the model in different experimental configurations that were used on the LVL QM and FM. The idea is to search for the values of the adjustable parameters that give the same horizontal resonance frequencies as in the laboratory data. To do this inversion, we randomly draw values for the adjustable parameters one million times and we calculate the χ^2 for each of these value sets as follows (Fig. 21):

$$\chi^2 = \frac{(f_{\text{model}} - f_{\text{data}})^2}{\sigma^2}, \quad (18)$$

where f_{model} and f_{data} represent the resonance frequencies calculated with the model and found in the experiment, respectively, and σ is the measurement uncertainty (equal to 0.3 Hz as discussed in Sect. 3.4). The results in Fig. 21 give a clear trade-off curve between the two parameters, and the best solutions are found around a curve which can be expressed as:

$$(k_h^g - A)(C_h^g - B) = AB$$

$$\frac{B}{C_h^g} + \frac{A}{k_h^g} = 1, \quad (19)$$

where A and B are constant found from data matching. This can be interpreted as a system where both the horizontal stiffness and the torque are in parallel for generating the tilt resonance.

As seen from Eq. (18), these parameters are directly related to both the Young's modulus and Poisson ratio and the numerical model presented here could be used to invert for ground properties at the InSight deployment site once SEIS data from Mars are available. However, the presence of the cone on the LVL's feet, which are not just circular disks, complicates the application of these formulas. Hence, more complete expressions are needed, which could be provided by additional experiments in which a model of the SEIS foot is penetrated into a Martian regolith simulant with a precise measurement of the axial force and elastic displacement once the foot is penetrated. On the other hand, thanks to Eq. (18), the ratio k_h^g/C_h^g can be determined solely depending on the Poisson ratio. Using a reasonable range of this coefficient (e.g. 0.1 to 0.4), this can already give narrow limits on the possible range of k_h^g vs. C_h^g values. This should be compared to the experimental results done with the real shape of the feet. Another possibility is to combine the results of this model with other experiments realized in order to determine the regolith properties of the InSight landing site (Golombek et al. 2018).

Results of the laboratory measurements show that in cases where the three legs are not of equal length (tilted LVL configurations), two different frequencies for the horizontal modes are observed (Table 1, lines 2 to 5). Depending on configuration, the resonances either do or do not align with the X- and Y-axes of the system. In this analytical model, we need to set different rigidity constants at ground level between the three legs to obtain two different frequency values for X and Y horizontal mode resonances. This would mean that the three feet couple to the ground differently. Things will then depend a lot on the actual deployment (i.e. local interaction between the feet and soil which is very hard to know) of SEIS on Mars. The fact that two frequencies with a difference of up to 1.8 Hz were not only observed with the LVL on sand, but also on rock (case number 2 of Table 1), may be explained by the fact that, depending on the test configuration, one or two feet were located on the sloping part of the rock, whereas the other feet were on the horizontal part. This could make a difference for the interaction between a foot and the ground.

5.2 6 Axes Seismometer Measurement with SEIS

As SEIS has 6 axes, measurements of both the vertical and horizontal accelerations at different distances from the center of mass of the LVL will be made. The three VBBs recompose for example the vertical axis in the center of the LVL while the vertical SP (noted SPZ) measures the vertical acceleration on the ring. Moreover, the three VBBs measure the horizontal acceleration at mid distance from the Sphere Center of Gravity, while the two horizontal SPs are again located just outside the ring, at a distance twice larger from the Sphere center. In addition and as noted by Forbriger (2009), VBBs are sensitive to the rotation rate with respect to their pendulum, as described in more detail in the [Appendix](#).

The 6 sensors can therefore sense the 6 axes of LVL acceleration and LVL rotation and SEIS is therefore able to work in a way similar to a rotaphone (Brokešová et al. 2012). But SEIS is reduced to the strict minimum number of sensors, has sensors sensitive to both acceleration and rotation (the 3 VBBs) and only acceleration (the 3 SPs) and was not originally designed for this purpose neither optimized in terms of sensors placement for rotation measurements nor calibrated with this goal. Figure 22 illustrates this concept for the three axes of rotation, and compares SEIS to a classical rotaphone.

Let us therefore discuss if SEIS can be considered, especially during the HP³ penetration, as the first device performing rotational seismology on a terrestrial body other than

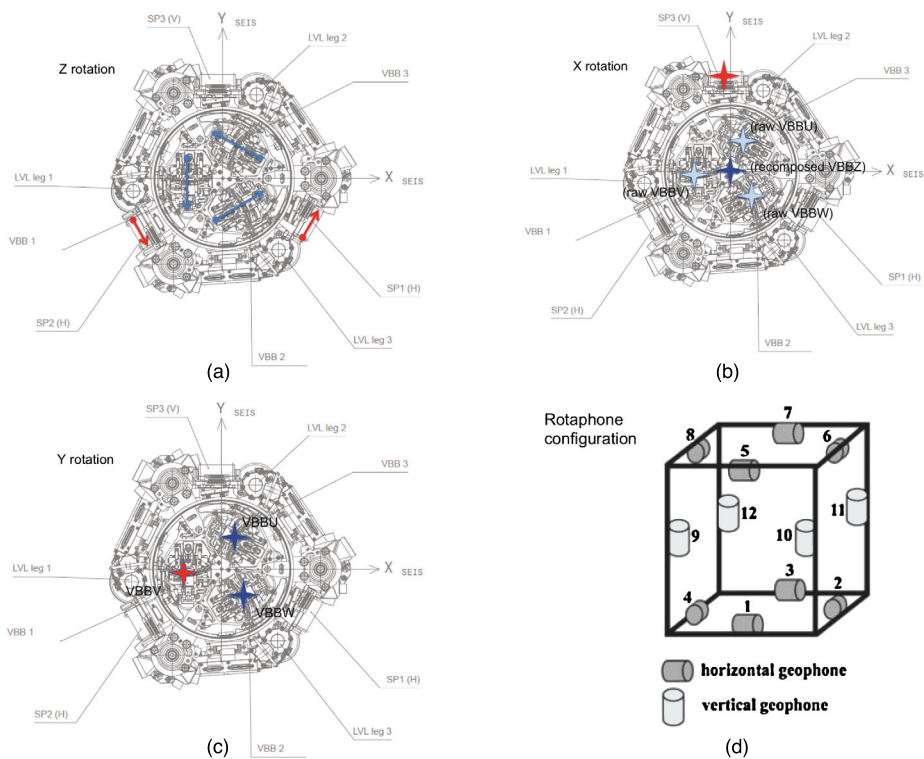


Fig. 22 Sketch for the rotation recombinations of the 6 axes. On (a), blue and red arrows represent the sensitivity axes of the VBBs and the SPs respectively. In (b), the stars are the different centers of mass (light blue for the VBBs, dark blue for the LVL, where the vertical sensitivity axis is recombined, and red for the vertical SP). In (c), rotation on one sense is represented in blue stars, and on the other sense in red stars. (a), (b) and (c) are respectively for Z, X and Y axes. The determination of rotation in Y is the least efficient due to the smaller distances between the different sensors sensitive to this rotation. For comparison, (d) shows the geometry of a rotaphone, reprinted from Brokešová et al. (2012), where rotation is not only obtained with optimized distances but also in a redundant way, enabling very precise calibration for the small differences associated to the dispersion of the transfer function of the sensors

Earth. See Igel et al. (2015) and Schmelzbach et al. (2018) for recent reviews on rotational seismology.

During the HP³ penetration, high frequency surface waves are indeed expected to be generated, especially at the beginning of the penetration, and the three feet of SEIS will be able to sample the surface displacement field on three locations far enough to have large phase differences in term of ground displacement. As described above, the distance between the acceleration measurement locations are about 10 cm and the distances between the feet are slightly more than 20 cm (see Fig. 2). SEIS will therefore be sensitive to the rotation effects associated with the gradient of the seismic waves at this distance. Because of the expected low shear wave (or the surface wave) velocity, of about 150 m/s for the surface materials (see Delage et al. 2017 for the mission ERD reference model and Morgan et al. 2018 for further discussion on the possible seismic velocity profiles near the surface), these 10 cm and 20 cm distances, therefore, correspond to about 1/30 and 1/15 of the wavelength at 50 Hz. At these frequencies, the measurements will therefore be closer to gradient analysis, already demonstrated on the Moon by Sollberger et al. (2016) but for the larger distances

between the lunar geophones deployed during the Lunar Seismic Profiling Experiment of Apollo 17.

Following Bernauer et al. (2009), let us first present the expected amplitude of the acceleration and rotation signals during the HP³ penetration. These will be used to compare the instantaneous rotation speed around the transverse component $\dot{\Omega}_\eta$ and the vertical acceleration obtained from the time differentiation of the platform center of mass velocity \dot{v}_z to determine the phase velocity c of the seismic wave induced by HP³ hammering, using this relation:

$$\dot{\Omega}_\eta = \frac{1}{c} \dot{v}_z. \quad (20)$$

To compute both the rotation and acceleration, we use the numerical simulation of the seismic signals generated by HP³ hammering. See Kedar et al. (2017) for the detail of this modeling, including the discussion on the separation of P and S waves in the expected signal. These simulations provide the radial and vertical displacement of the ground at the LVL's feet number 1, 2 and 3, for geometries where feet 2 and 3 are at the same distance from HP³ and for a defined distance and depth of the HP³ mole. These synthetic seismic waves were made assuming a cylindrical source (e.g. vertical penetration of the mole) and a 1D seismic structure.

The $\dot{\Omega}_\eta$ instantaneous rotation speed, defined by Eq. (20), were calculated by finite differences on the vertical ground velocity taken between the feet locations:

$$\dot{\Omega}_\eta = \frac{\partial v_z}{\partial x} \sim \frac{\Delta v_z}{\Delta x}, \quad (21)$$

while the vertical velocity v_z (derivative of the displacement u_z) is determined as the mean velocity of the three feet which is therefore computed at the center of the three feet. All these fields are provided by the HP³ simulation displacement data converted into ground velocity or acceleration. The simulations used here are those at low HP³ penetration depth, for which the surface waves are the strongest.

We used then the model describing the translation of the LVL CoG and the rotation of the LVL axes frame (as given by Eqs. (1) and (8)) and expressed the absolute velocity of each sensor at the center of gravity of their inertial mass with both the LVL CoG translational velocity and the rotation speed with the companion expression of Eq. (6):

$$\vec{v}_i \cdot \vec{n}_i = [\vec{v}_F + \vec{\Omega}_F \times \vec{G}_p \vec{S}_i] \cdot \vec{n}_i, \quad (22)$$

where $\vec{\Omega}_F$ is the platform angular instantaneous rotation speed of the LVL frame, \vec{v}_F the LVL translational speed, i denotes one of the 6 axes, \vec{n}_i is the sensing direction of the component i and $\vec{G}_p \vec{S}_i$ the vector between the platform Center of Gravity and the Center of Gravity of the proof mass of component i .

This allowed us to estimate the transfer matrix between the 6 axes LVL velocity and instantaneous rotation speed vectors and the 6 axes outputs recorded by both the SPs and the VBBs, which provide the sensor absolute velocities, as recorded on the location of their proof mass. Note that we do integrate, for the VBBs, their rotation sensibility following expressions of the Appendix. In this process, we fully modeled the SEIS acquisition system, including the SEIS-AC decimation filter.

The upper part of Fig. 23 shows the amplitudes expected for the ground acceleration and rotation, for 30–40 Hz and 10–20 Hz 5th order butterworth band pass filtered signals. Phase velocities of about 131 m/s and 141 m/s are found by least-square fitting by using

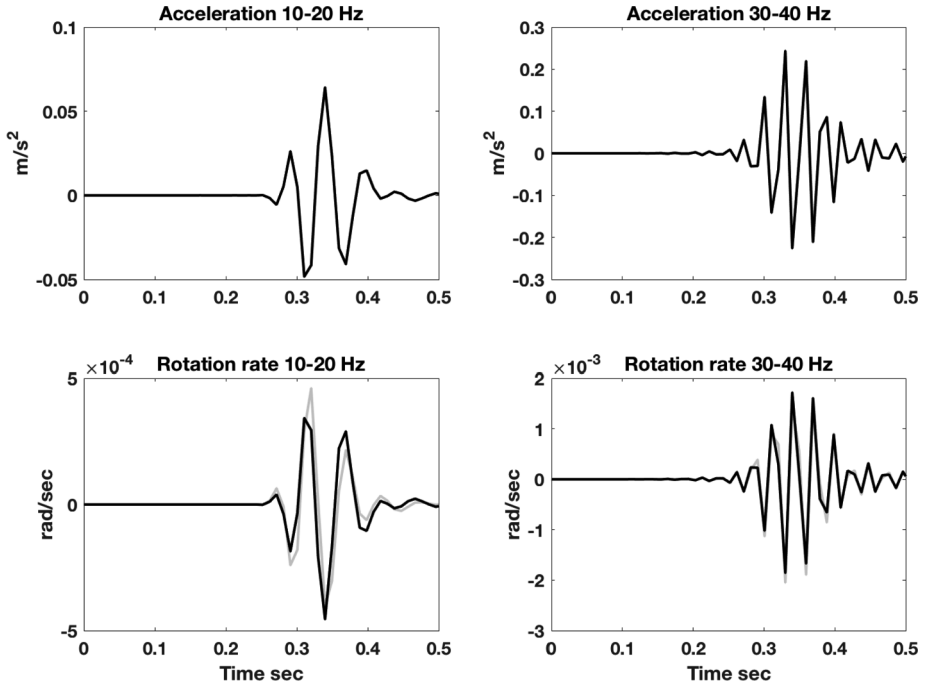


Fig. 23 Mean acceleration at the LVL center of mass (top figure) and transverse LVL rotation (bottom figures), after a simulated penetration of HP^3 . On the left, data have been filtered between 10 and 20 Hz, while at the right, the bandwidth was 30–40 Hz. The lower figures represent the comparison between the vertical velocities determined by the two different methods cited in the text: thanks to the acceleration in black and the rotation in grey

Eq. (20). Note that SEIS is however close from the source, the distance between two feet is about 15–20% of the propagation distance d and a large geometrical spreading is found, with amplitudes decaying as $\frac{1}{\sqrt{d}}$, preventing the direct use of Eq. (20) which is only valid for a plane wave far from the source. For this reason, a geometric correction was applied in the computation of the instantaneous rotation from Eq. (21) but we get nevertheless phase velocities still lower than the used one in the simulations. Moreover, the ground attenuation is also affecting the results, but less significantly than the Rayleigh pole, which gives about 160 m/s for the model used by Kedar et al. (2017) in its simulation. A better understanding of the phase velocity in very close field and for attenuating waves is requested for interpreting these phase velocities but is not central to this study which is focused on the impact of the calibration errors. The lower part of Fig. 23 shows the result of the comparison between the velocities determined by two different methods: the mean velocity at the center of the three feet with a phase velocity inverted by a least-squares approach from fitting the waveform bandpassed at high frequencies.

As indicated above however, the flight models of the sensors have however not been calibrated for such measurements; Earth’s gravity prevented indeed the simultaneous operation of all 6 sensors on Earth. This will therefore prevent us of using SEIS as a well calibrated rotation sensor.

The actual transfer function will therefore be only estimated from computer assisted design models providing the precise location of the center of gravity of the 6 proof masses in

Table 3 Summary of the calibration errors assumed in the known position of the VBBs and SPs mobile mass center of gravity, in the dip and azimuth directions, in the VBBs to SPs relative transfer functions and VBBs rotation sensitivity

VBB parameter	VBB position	VBB azimuth	VBB dip	VBB transfer function	VBB rotation sensitivity
Error	500 μm	0.05 $^\circ$	0.1 $^\circ$	0.25%	5%
SP parameter	SP position	SP azimuth	SP dip	SP transfer function	SP rotation sensitivity
Error	250 μm	0.05 $^\circ$	0.05 $^\circ$	0.25%	None

the LVL frame and from precise calibration of the sensors. We expect to complete these calibration informations, during Mars operations, by dedicated cross-calibration of the VBBs and SPs. The first calibration will be performed with the LVL system, where tilt signals will be generated by moving the LVL legs. This will mostly excite tilt and therefore rotation. The second calibration will be continuous operation of the VBBs and SPs during one month which will allow precise relative cross-correlation of the VBBs with respect to SPs through the recording of Mars micro-seismic noise and possibly seismic signals. We expect that most of the signal will in this case be LVL translation.

In order to illustrate the calibration limitations, we have run a random exploration of the impact of the transfer function errors, by introducing errors in the different parameters affecting the transfer matrix between the 6 SEIS axes and the 6 acceleration+rotation axes. In that test, the errors amplitudes are listed in Table 3. The sensitivity of the VBBs to rotation is expressed in the [Appendix](#).

The calibration errors are generating noise on the rotation recovery depending on the signal. This calibration noise is much larger than the self noise of the 6 sensors, when expressed in terms of acceleration and rotation measurement noise and will likely be also much larger than the high frequency natural noise, due to the very large amplitude of the HP³ signal. As suggested by the SEIS noise model (Mimoun et al. 2017), the high frequency noise is indeed expected to be dominated by the sensor self noise. Figure 24 shows the signal spectrum, for the two vertical and longitudinal components of acceleration and the two rotation ones, transverse and vertical. This is illustrated in the two bandwidth (10–20 Hz and 30–40 Hz). Typically, the rotation spectrum can be recovered with about 10% while the acceleration is recovered with 0.35%. Note that when the source geometry is known, and especially for the HP³ signal, which is expected to have a cylindrical geometry and a known surface waves ray, the transfer function error can be furthermore constrained by assuming the radial rotation to cancel. We also note that the error grows rapidly at low frequency, suggesting that the rotation analysis will likely be possible only at frequencies larger than 10 Hz.

These calibration errors will nevertheless obviously directly impact the measurements of the phase velocity. This is illustrated by Fig. 25, which shows for the bandpass 30–40 Hz the noise associated to the calibration errors and results for the two frequencies are shown on Fig. 26. We note that the largest sources of errors are the dip angle of the VBBs and the calibration errors of both SPs and VBBs, which are expected to be much better known after the on Mars calibration and commissioning. We expect the dip angles to have no frequency dependancy and the High Frequency Gain error to be weakly frequency dependant. This suggests therefore that the measurement of the frequency variation of the phase velocity, which will directly be related to the variation of the seismic velocities with depth, will be less affected and could be determined, with perspectives of inversion of the subsurface structure.

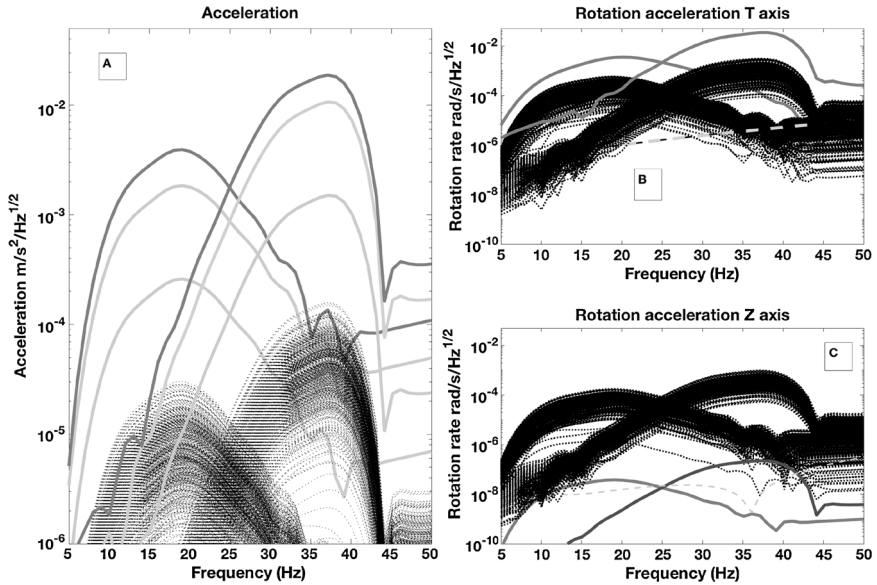


Fig. 24 Signal and calibration errors for the HP³ signals in the frequency domain for the two bandwidths tested (10–20 Hz and 30–40 Hz). Acceleration is on the left figure (A) where dark grey is the Z axis signal and light grey the Longitudinal axis signal. Fields are rotated with respect to the HP³ location: the azimuth of HP³ is 8° with respect to the center of SEIS, while the azimuth of the 3 SEIS feet are respectively -172° , 68° and -52° . The azimuth of the feet from HP³ are therefore 8° , 13.8° and 2.2° respectively. The thin lines are the acceleration calibration error. (B) shows the Transverse rotation, associated to surface waves, while (C) shows the vertical rotation. The continuous large line is the signal, while the thin lines are the calibration noise obtained for 200 random values of the transfer function. The dashed grey lines are the sensors self noise. In the worst case, the rotation is measured with 10% of the calibration noise

To summarize, we do believe that SEIS will be able to measure, during the HP³ penetration, the ground translation and rotation independently at frequencies larger than 5–10 Hz and for near surface Rayleigh waves. The determination of the transfer function will be one of the challenges of the experiment. The existing knowledge of these transfer function is described by Lognonné et al. (2018) and will be described in the SEED dataless provided with the data. The first delivery, expected in spring 2019, will be based on the prelaunch calibration while the second delivery, in summer 2019 will likely integrate the post-landing calibration process, as well as the data gathered during the HP³ penetration phase.

Assuming that all components are operational, the 6 axes SEIS instrument will allow, as predicted by the rotational seismology (Eq. (20)), the determination of the surface waves' phase velocity (Bernauer et al. 2009). Further analysis will be made to assess if the 6 axes analyses can be used also for separating the different phases of the HP³ signals, including differences between the P converted SV reflected phase and the SV and SH incident phases, as the latter are weakly resolved by the low sampling rate of the experiment and can also be envisaged for micro-seismic noise analysis.

6 Data Filtering

Even if the SP has a flat ground velocity output up to kHz, the only two sampling options are 20 sps and 100 sps. In normal operation, the digitized seismic recordings will therefore

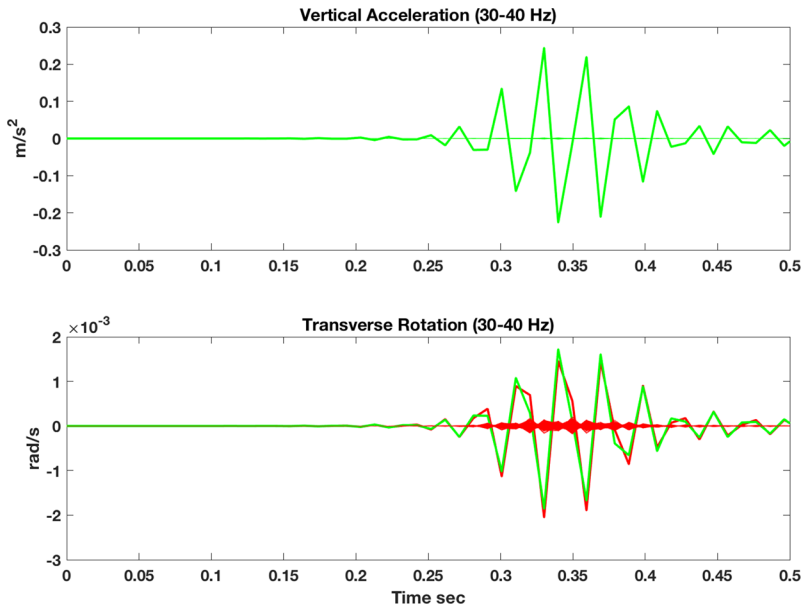
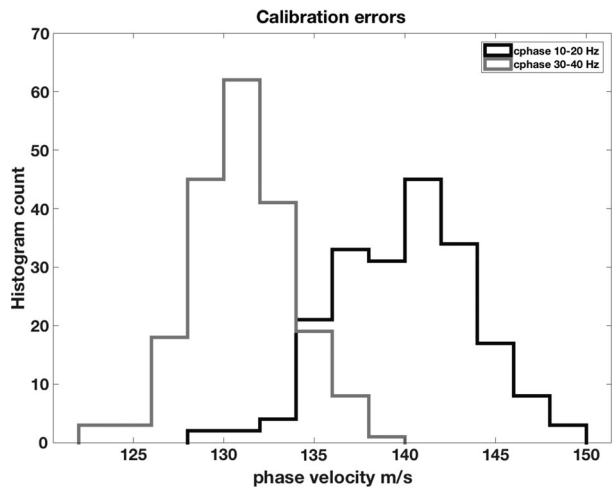


Fig. 25 Calibration errors for the HP³ signals in the time domain. On the top in green is the vertical acceleration, as acquired at 100 sps and with 30–40 Hz bandpass filter. Green traces near the X axis are corresponding to the calibration noise. On the bottom is the rotation rate (red) and its comparison with the computed rate for the acceleration and phase velocity around 131 m/s (green). See Fig. 26 for the histograms. Red traces near the X axis are corresponding to the calibration noise

Fig. 26 Histograms of the phase velocities for the 30–40 Hz low passed data (left) and the 10–20 Hz ones (right), with the dispersion of the calibration used for the random exploration. $\pm 5\%$ dispersion is found



be passed through a cascaded sequence of antialiasing FIR filters followed by subsampling to downsample the data from initially 500 sps to either 100 sps or smaller sampling rates. As a consequence, energy above 50 Hz will be either lost by the anti-aliased filter, or signal will be aliased if no filter is implemented prior the 100 sps acquisition.

Studying resonances of the LVL at high frequencies (< 250 Hz) will however be possible for the time period of the HP³ experiment during which data with the full bandwidth sampled

at 500 sps can be recovered. The proposed strategy is to exploit the observation that the HP³ seismic data are characterized by a high number of very similar signals generated by each mole hit and the fact that the hammering is not synchronized with the seismic data sampling. This allows to use compressive sensing techniques to recover signals (e.g. HP³ hammer strokes, LVL resonances) for the entire bandwidth up to 500 sps (Schmelzbach et al. 2018, in preparation).

7 Conclusion

We determined the transfer function of the SEIS LVL, which is the last part of the seismic transfer of the signal between the Martian surface and the 6 axis accelerometer made by the 3 VBBs and 3 SPs. This was made with a 4 masses, spring coupled, model of the LVL, representing the 3 feet and the LVL platform, and with feet coupling integrating both the vertical and horizontal response of the ground. We have shown that in the seismic bandwidth of the instrument, the major impact of the LVL on the seismic signal will be associated to the oscillation modes of the almost rigid LVL placed on the low rigidity ground, which will generate both a seismic resonance and a signal cutoff at frequencies ranging from 20 to 40 Hz, depending on the rigidity of the ground. The model fits well all the data acquired during the tests processes, for both the QM and FM and will be incorporated into the final transfer function of SEIS in the dataless SEED provided for the full instrument transfer function documentation.

The validation of the model has shown that the two associated horizontal resonances are highly dependent on ground properties, especially the horizontal stiffness k_h^g and the torque C_h^g . This opens the possibility to invert these parameters for better constraining the Martian ground rheology and this inversion will be made with the first data acquired during the SEIS commissioning on Mars. We illustrated the perspectives by performing a first inversion of the test data and demonstrating the trade-off between these two parameters. The parameter space might be reduced by determining the link between the Poisson coefficient and Young's modulus on one side, and the feet disk radius of the LVL feet, C_h^g and k_h^g on the other side. We illustrated this link with the analytical solutions associated to flat feet and will develop them further by integrating the conic spike of the actual feet in the mathematical formulation. These improvements will be achieved during cruise by both finite elements modeling and laboratory measurements. Another upgrade of the model will be the inclusion of the LSA and tether. The LSA can be considered as an additional mass on the side of the LVL ring, which could slightly change its transfer function. Its integration in the model will therefore be performed, again to be validated with the laboratory experiments.

As SEIS has 6 axes for the seismic signal measurement and thanks to the different positions of the VBBs and SPs from the LVL Center of mass, both seismic acceleration and rotation can be measured, as predicted by the rotational seismology. We proposed to record the high frequency surface waves generated by HP³ hammering in order to determine their phase velocity. However, the flight model of the SEIS instrument has not been calibrated for such measurement. The calibration limitations were illustrated thanks to the run of a random exploration of transfer function errors and by using the simulated HP³ seismic signals. Finally, after introducing errors in the different parameters affecting the transfer matrix between the 6 SEIS axes and the 6 acceleration and rotation axes, we noticed that the rotation is measured with 10% of the calibration noise in the worst case. Nevertheless, the largest error sources are the dip angle of the VBBs and the calibration errors of both SPs and VBBs,

which are expected to be much better known after calibration on Mars. Moreover, the measurement of the phase velocity frequency variation will be directly related to the variation of the seismic velocities with depth. This will allow to invert the martian subsurface structure thanks to the HP³ hammering seismic signals at frequencies larger than 10 Hz.

Acknowledgements This is IGP contribution xx and InSight contribution yy. L.F. acknowledges the financial support of ANR-11-IDEX-0005-02 and the additional support of ANR-SIMARS F.K. acknowledges the financial support of the UnivEarthS Labex program at Sorbonne Paris Cité (ANR-10-LABX-0023 and ANR-11-IDEX-0005-02) and of the SODERN company for his Ph.D. support. The French team acknowledges the support of the French Space Agency CNES for the overall SEIS developments.

Appendix: Rotation Sensitivities of the VBB Sensors

As shown by Forbriger (2009), pendulum and therefore VBBs have a rotational sensitivity in addition of their acceleration sensitivity along their sensitivity direction. VBBs are in addition oblique sensors and use gravity to lower their eigenfrequency and increase their mechanical sensitivity, which must also be taken into account.

Let us consider one of the VBB sensor and note G its center of mass and M a part of the proof mass. The acceleration sensed by the point M can be expressed as

$$\frac{d^2 \overrightarrow{OM}}{dt^2} = \overrightarrow{\gamma} + \overrightarrow{\dot{\Omega}} \times \overrightarrow{OM} + \overrightarrow{\Omega} \times [\overrightarrow{\Omega} \times \overrightarrow{OM}] \quad (23)$$

where $\overrightarrow{\gamma}$ is the acceleration of the VBB pivot and $\overrightarrow{\dot{\Omega}}$ is the absolute rotation rate with respect to a fixed frame and $\overrightarrow{\Omega}$ the rotation acceleration. $\overrightarrow{\Omega}$ is therefore the sum of the LVL rotation, noted hereafter $\overrightarrow{\Omega}_F$ and of the VBB pendulum rotation, noted $\theta \overrightarrow{\pi}$ where $\overrightarrow{\pi}$ the pivot directed vector (in trigonometric direction) and θ is the rotation of the pendulum with respect to the equilibrium and recentered position. If we limit this expression to only the first order linear term, assuming the rotation to remain small due to the pendulum restoring forces, we can express the acceleration of M

$$\frac{d^2 \overrightarrow{OM}}{dt^2} = \overrightarrow{\gamma} + \overrightarrow{\dot{\Omega}} \times \overrightarrow{OM}_0 = \ddot{\theta} \overrightarrow{\pi} \times \overrightarrow{OM}_0 + \overrightarrow{\gamma}_G + \overrightarrow{\dot{\Omega}}_F \times \overrightarrow{G}_0 M_0 \quad (24)$$

where G_0 and M_0 are now the center of gravity of the mobile mass and point M both taken in their equilibrium positions. $\ddot{\theta}$ is the second derivative of θ , $\overrightarrow{\dot{\Omega}}_F$ the rotation acceleration along the pivot direction and $\overrightarrow{\gamma}_G$ is the full acceleration (including frame rotation) at the equilibrium center of gravity G_0 . By assuming that the pendulum of the VBB has one of its inertial moment axis along the pivot and computing the equation of angular momentum with respect to rotation around the pivot, we can finally write the pendulum equation of movement as:

$$J\ddot{\theta} = \mathcal{M}_0 - C\theta - C_R\theta + m(\overrightarrow{OG} \times \overrightarrow{g}).\overrightarrow{\pi} - [m(\overrightarrow{OG}_0 \times \overrightarrow{\gamma}_G).\overrightarrow{\pi} + (J - mD^2)\ddot{\Omega}_F], \quad (25)$$

where \mathcal{M}_0 is the spring moment at recentered position, J is the VBB moment of inertia with respect to the pivot, C the spring/pivot stiffness, C_R the feedback force (as a function of the pendulum rotation), \overrightarrow{g} the Mars gravity and D the distance from pivot to center of gravity. Note that when the VBB is perturbed, G is moving such that:

$$\overrightarrow{OG} = \overrightarrow{OG}_0 + \theta \overrightarrow{\pi} \times \overrightarrow{OG}_0 = D[\overrightarrow{\pi} + \theta \overrightarrow{\pi}], \quad (26)$$

where \vec{n} is the direction sensitivity vector. When the infinitesimal rotation $\vec{\Omega}$ is perturbing the VBB in addition to ground acceleration, the local gravity is changing. If we rewrite the previous equation in the moving frame of the VBB sensor, the gravity can then be written as

$$\vec{g} = \vec{g}_0 - \vec{\Omega} \times \vec{g}_0. \quad (27)$$

These two equations leads to the pendulum dynamic equation. When we note that

$$\mathcal{M}_0 + m(\vec{OG}_0 \times \vec{g}_0) \cdot \vec{\pi} = 0, \quad (28)$$

this can be rewritten as:

$$\begin{aligned} J\ddot{\theta} + [C - mD(\vec{n} \times \vec{g}_0) \cdot \vec{\pi} + C_R]\theta \\ = -mD\vec{p} \times [\vec{\Omega} \times \vec{g}_0 + \vec{\gamma}_G] \cdot \vec{\pi} - (J - mD^2)\ddot{\Omega}_F, \end{aligned} \quad (29)$$

$$\begin{aligned} J\ddot{\theta} + [C - mD(\vec{n} \times \vec{g}_0) \cdot \vec{\pi} + C_R]\theta \\ = -mD[\vec{p} \cdot \vec{g}_0 \vec{\Omega}_F + \vec{\gamma}_G \cdot \vec{n}] - (J - mD^2)\ddot{\Omega}_F, \end{aligned} \quad (30)$$

$$\begin{aligned} J\ddot{\theta} + [C - mD \cos \alpha + C_R]\theta \\ = -mD \left[\vec{\gamma}_G \cdot \vec{n} + \frac{J - mD^2}{mD^2} D\ddot{\Omega}_F - g_0 \cos \alpha \Omega_F \right], \end{aligned} \quad (31)$$

where α is the angle of \vec{p} with vertical (see Fig. 37 of Lognonné et al. 2018 for VBB pendulum geometry). The amplitude of the first rotation term is related to the non-point character of the pendulum. For the VBBs family, we have $J = 2.56 \times 10^{-4} \text{ kg m}^2$, $D = 0.0256 \text{ m}$ and $m = 190 \text{ g}$ and therefore $\frac{J - mD^2}{mD^2}$ is about 1.06. For a rotation acceleration of about $\ddot{\Omega}_F = \omega \frac{z_c}{c}$, where ω is the angular frequency and c the wave phase velocity, the ratio of the second term to acceleration is $\frac{D\omega}{c \sin \alpha} = 2\%$ for 10 Hz and $c = 150 \text{ m/s}$. This is therefore significant but does not request more than 5% of moment of inertia or location of center of gravity errors to generate errors of less than 0.1%. The third term is small and for seismic waves detection the ratio between rotation term and acceleration is of the order of $\frac{g_0}{\tan \alpha \omega c}$. On Mars, the last term will be smaller than 10^{-3} for frequencies larger than 7 Hz and phase velocity of 150 m/s. This is expected to be significantly lower than the calibration error of the VBBs and SPs and we can therefore neglect this third rotation sensitivity term of the VBBs for the HP³ surface waves signals in our simulation, which are expected in the 10–50 Hz bandwidth.

References

- D.L. Anderson, W.F. Miller, G.V. Latham, Y. Nakamura, M.N. Toksöz, A.M. Dainty, F.K. Duennebieer, A.R. Lazarewicz, R.L. Kovach, T.C.D. Knight, Seismology on Mars. *J. Geophys. Res.* **82**, 4524–4546 (1977)
- C. Bagaini, C. Barajas-Olalde, Assessment and compensation of inconsistent coupling conditions in point-receiver land seismic data. *Geophys. Prospect.* **55**, 39–48 (2007). <https://doi.org/10.1111/j.1365-2478.2006.00606.x>
- W.B. Banerdt, S. Smrekar, K. Hurst, P. Lognonné, T. Spohn, S. Asmar, D. Banfield, L. Boschi, U. Christensen, V. Dehant, W. Folkner, D. Giardini, W. Goetz, M. Golombek, M. Grott, T. Hudson, C. Johnson, G. Kargl, N. Kobayashi, J. Maki, D. Mimoun, A. Mocquet, P. Morgan, M. Panning, W.T. Pike, J. Tromp, T. van Zoest, R. Weber, M. Wieczorek (the InSight Team), Insight: a Discovery mission to explore the interior of Mars, in *Proc. 44th Lunar Planet. Sci. Conf., Lunar and Planetary Institute*, Houston (2013), p. 115

-
- M. Bernauer, A. Fichtner, H. Igel, Inferring Earth structure from combined measurements of rotational and translational ground motions. *Geophysics* **74**(6), WCD41–WCD47 (2009). <https://doi.org/10.1190/1.3211110>
- J. Brokešová, J. Málek, J.R. Evans, Note: Rotaphone, a new self-calibrated six-degree-of-freedom seismic sensor. *Rev. Sci. Instrum.* **83**(8), 086108 (2012)
- CNES, Internal M-ICD (Mechanical Interface Control Document) of SEIS instrument of InSight mission (2017)
- S. De Raucourt, T. Gabsi, N. Tanguy, D. Mimoun, P. Lognonne, J. Gagnepain-Beyneix, W. Banerdt, S. Tillier, K. Hurst, The VBB SEIS experiment of InSight, in *39th COSPAR Scientific Assembly, COSPAR Meeting*, vol. 39 (2012), p. 429
- P. Delage, F. Karakostas, A. Dhemaied, M. Belmokhtar, P. Lognonné, M. Golombek, E. De Laure, K. Hurst, J.-C. Dupla, S. Kedar, Y.J. Cui, B. Banerdt, An investigation of the mechanical properties of some Martian regolith simulants with respect to the surface properties at the InSight mission landing site. *Space Sci. Rev.* **211**, 191–213 (2017). <https://doi.org/10.1007/s11214-017-0339-7>
- T. Forbriger, About the nonunique sensitivity of pendulum seismometers to translational, angular, and centripetal acceleration. *Bull. Seismol. Soc. Am.* **99**, 1343–1351 (2009). <https://doi.org/10.1785/0120080150>
- M. Golombek, D. Kipp, N. Warner, I.J. Daubar, R. Ferguson, R. Kirk, R. Beyer, A. Huertas, S. Piqueux, N. Putzig, B.A. Campbell, G.A. Morgan, C. Charalambous, W.T. Pike, K. Gwinner, F. Calef, D. Kass, M. Mischna, J. Ashley, C. Bloom, N. Wigton, T. Hare, C. Schwartz, H. Gengl, L. Redmond, M. Trautman, J. Sweeney, C. Grima, I.B. Smith, E. Sklyanskiy, M. Lisano, J. Bernardini, S. Smrekar, P. Lognonné, B. Banerdt, Selection of the InSight landing site. *Space Sci. Rev.* **211**, 5–95 (2017). <https://doi.org/10.1007/s11214-016-0321-9>
- M. Golombek, M. Grott, G. Kargl, J. Andrade, J. Marshall, N. Warner, N.A. Teanby, V. Ansan, E. Hauber, J. Voigt, R. Lichtenheldt, B. Knapmeyer-Endrun, I.J. Daubar, D. Kipp, N. Muller, P. Lognonné, C. Schmelzbach, D. Banfield, A. Trebi-Ollennu, J. Maki, S. Kedar, D. Mimoun, N. Murdoch, S. Piqueux, P. Delage, W.T. Pike, C. Charalambous, R. Lorenz, L. Fayon, A. Lucas, S. Rodriguez, P. Morgan, A. Spiga, M. Panning, T. Spohn, S. Smrekar, T. Gudkova, R. Garcia, D. Giardini, U. Christensen, T. Nicollier, D. Sollberger, J. Robertsson, K. Ali, B. Kenda, W.B. Banerdt, Geology and physical properties investigation by the InSight lander. *Space Sci. Rev.* **214**(5), 1–52 (2018). <https://doi.org/10.1007/s11214-018-0512-7>, 2nd special issue
- L.G. Holcomb, A direct method for calculating instrument noise levels in side-by-side seismometer evaluation (1989). Open File Rep. 89-214, U.S. Geol. Surv.
- H. Igel, M. Bernauer, J. Wassermann, K.U. Schreiber, Rotational seismology: theory, instrumentation, observations, applications, in *Encyclopedia of Complexity and Systems Science* (Springer, New York, 2015)
- S. Kedar, J. Andrade, B. Banerdt, P. Delage, M. Golombek, M. Grott, T. Hudson, A. Kiely, M. Knapmeyer, B. Knapmeyer-Endrun, C. Krause, T. Kawamura, P. Lognonné, T. Pike, Y. Ruan, T. Spohn, N. Teanby, J. Tromp, J. Wookey, Analysis of regolith properties using seismic signals generated by InSight's HP³ penetrator. *Space Sci. Rev.* **211**, 315–337 (2017). <https://doi.org/10.1007/s11214-017-0391-3>
- B. Knapmeyer-Endrun, N. Murdoch, B. Kenda, M.P. Golombek, M. Knapmeyer, L. Witte, N. Verdier, S. Kedar, P. Lognonné, W.B. Banerdt, Influence of body waves, instrumentation resonances, and prior assumptions on Rayleigh wave ellipticity inversion for shallow structure at the insight landing site. *Space Sci. Rev.* **214**(5), 1–42 (2018), 2nd special issue
- P. Lognonné, W.T. Pike, *Planetary Seismometry* (Cambridge University Press, Cambridge, 2015)
- P. Lognonné, J.G. Beyneix, W.B. Banerdt, S. Cacho, J.F. Karczewski, M. Morand, Ultra broad band seismology on InterMarsNet. *Planet. Space Sci.* **44**, 1237 (1996). [https://doi.org/10.1016/S0032-0633\(96\)00083-9](https://doi.org/10.1016/S0032-0633(96)00083-9)
- P. Lognonné, B.W. Banerdt, D. Giardini, T. Pike, U. Christensen, P. Laudet, S. de Raucourt, P. Zweifel, S. Calcut, M. Bierwirth, K. Hurst, F. Ijpelaan, J. Umland, R. Roger Llorca, S. Larson, R. Garcia, S. Kedar, B. Knapmeyer-Endrun, D. Mimoun, A. Mocquet, M. Panning, R. Weber, A. Sylvestre-Baron, G. Pont, N. Verdier, L. Kerjean, T. Hoffman, J. Willis, S. Smrekar, M. Eberhardt, A. Kramer, W. Kühne, E.-P. Miettinen, M. Monecke, J.P. Scheffler, C. Aicardi, K. Brethomé, C. Brysbaert, T. Carlier, J.M. Desmarres, D. Faye, R. Gonzalez, L. Luno, J.M. Mouret, M. Nonon, A. Paillet, G. Perez, B. Pouilloux, A. Rosak, I. Savin de Larclause, N. Toulemon, B. Vella, C. Yana, P. Delage, L. Fayon, N. Murdoch, R. Widmer-Schmidrig, SEIS: the Seismic Experiment for Internal Structure of InSight. *Space Sci. Rev.* (2018), 2nd special issue
- D. Mimoun, N. Murdoch, P. Lognonné, K. Hurst, W.T. Pike, J. Hurley, T. Nébut, W.B. Banerdt, The noise model of the SEIS seismometer of the InSight Mission to Mars. *Space Sci. Rev.* **211**, 383–428 (2017). <https://doi.org/10.1007/s11214-017-0409-x>
- P. Morgan, M. Grott, B. Knapmeyer-Endrun, M. Golombek, P. Delage, P. Lognonné, S. Piqueux, I. Daubar, N. Murdoch, C. Charalambous, W.T. Pike, N. Muller, A. Hagermann, M. Siegler, R. Lichtenheldt, N.

-
- Teanby, S. Kedar, A pre-landing assessment of regolith properties at the insight landing site. *Space Sci. Rev.* **214**(6), 1–47 (2018), 2nd special issue
- R. Myhill, N. Teanby, J. Wookey, Frequency dependence of seismic attenuation and coupling through Mars' regolith: implications for the InSight mission. *Space Sci. Rev.* (2018). <https://doi.org/10.1007/s11214-018-0514-5>, 2nd special issue
- Y. Nakamura, D.L. Anderson, Martian wind activity detected by a seismometer at Viking lander 2 site. *Geophys. Res. Lett.* **6**, 499–502 (1979)
- G.L. Pavlis, F.L. Vernon, Calibration of seismometers using ground noise. *Bull. Seismol. Soc. Am.* **84**, 1243–1255 (1994)
- G.H. Peters, W. Abbey, G.H. Bearman, G.S. Mungas, J.A. Smith, R.C. Anderson, S. Douglas, L.W. Beegle, Mojave Mars simulant—characterization of a new geologic Mars analog. *Icarus* **197**, 470–479 (2008). <https://doi.org/10.1016/j.icarus.2008.05.004>
- H.G. Poulos, E.H. Davis, *Elastic Solutions for Soil and Rock Mechanics* (Wiley, New York, 1974)
- A.T. Ringer, C.R. Hutt, J.R. Evans, L.D. Sandoval, A comparison of seismic instrument noise coherence analysis techniques. *Bull. Seismol. Soc. Am.* **101**, 558–567 (2011)
- C. Schmelzbach, S. Donner, H. Igel, D. Sollberger, T. Taufiqurrahman, F. Bernauer, M. Hausler, C. Van Renterghem, J. Wassermann, J. Robertsson, Advances in 6-C seismology: applications of combined translational and rotational motion measurements in global and exploration seismology. *Geophysics* **83**, Issue(3), 1–58 (2018). <https://doi.org/10.1190/geo2017-0492.1>
- D. Sollberger, C. Schmelzbach, J.O.A. Robertsson, S.A. Greenhalgh, Y. Nakamura, A. Khan, The shallow elastic structure of the lunar crust: new insights from seismic wavefield gradient analysis. *Geophys. Res. Lett.* **43**, 10 (2016). <https://doi.org/10.1002/2016GL070883>
- D. Sollberger, S.A. Greenhalgh, C. Schmelzbach, C. Van Renterghem, J.O.A. Robertsson, 6-C polarization analysis using point measurements of translational and rotational ground-motion: theory and applications. *Geophys. J. Int.* **213**, 77–97 (2018). <https://doi.org/10.1093/gji/ggx542>
- P. Spudich, L.K. Steck, M. Hellweg, J.B. Fletcher, L.M. Baker, Transient stresses at Parkfield, California, produced by the M 7.4 Landers earthquake of June 28, 1992: observations from the UPSAR dense seismograph array. *J. Geophys. Res.* **100**, 675–690 (1995). <https://doi.org/10.1029/94JB02477>
- N. Teanby, J. Stevanović, J. Wookey, N. Murdoch, J. Hurley, R. Myhill, N.E. Bowles, S.B. Calcutt, W.T. Pike, Seismic coupling of short-period wind noise through Mars' regolith for NASA's InSight lander. *Space Sci. Rev.* **211**, 485–500 (2017). <https://doi.org/10.1007/s11214-016-0310-z>
- N.H. Warner, M.P. Golombek, J. Sweeney, R. Fergason, R. Kirk, C. Schwartz, Near surface stratigraphy and regolith production in southwestern Elysium Planitia, Mars: Implications of Hesperian-Amazonian terrains and the InSight lander mission. *Space Sci. Rev.* **211**, 147–190 (2017). <https://doi.org/10.1007/s11214-017-0352-x>